

The inter-scale energy budget in a von Kármán mixing flow

Anna N. Knutsen¹†, Pawel Baj¹, John M. Lawson^{2,3}, Eberhard Bodenschatz², James R. Dawson¹, and Nicholas A. Worth¹

¹Department of Energy and Process Engineering, Norwegian University of Science and Technology, Trondheim, Norway

²Max Planck Institute of Dynamics and Self-Organisation, Göttingen, Germany

³Department of Fluid Dynamics, University of Southampton, Southampton, United Kingdom

(Received xx; revised xx; accepted xx)

A detailed assessment of the inter-scale energy budget of the turbulent flow in a von Kármán mixing tank has been performed based on two extensive experimental data sets. Measurements were performed at $Re_\lambda = 199$ in the central region of the tank, using Scanning PIV to fully resolve the velocity gradient tensor (VGT), and Stereoscopic PIV for an expanded field of view (FoV). Following a basic flow characterization, the Kármán-Howarth-Monin-Hill equation was used to investigate the inter-scale energy transfer. Access to the full VGT enabled the contribution of the different terms of the energy budget to be evaluated without any assumptions or approximations. The scale-space distribution of the dominant terms was also reported to assess the isotropy of the energy transfer. The results show a highly anisotropic distribution of energy transfer in scale-space. Energy transfer was shown in an spherical averaged sense to be dominated at the small-scales by the non-linear inter-scale transfer term. However, in contrast to flows considered in previous studies, the local energy transfer is found to depend heavily on the linear contribution associated with the mean flow. Analysis of the scale-to-scale transfer of energy also allowed direct assessment of the classical picture of the energy cascade. It was found that while the inter-scale energy cascade driven by the turbulent fluctuations always proceeds in the forward direction, the total energy cascade driven by both the turbulent fluctuations and the mean flow exhibits significant inverse cascade regions, where energy is transferred from smaller to larger scales.

1. Introduction

Turbulent flows are characterised by their unsteady, three-dimensional motion across a wide range of length and time scales. The observation of small scale motion in flows containing energy injection at only the large scale prompted the classical concept of an energy cascade (Richardson 1926), where energy is transferred to increasingly fine scale motion, until viscosity finally limits the process through dissipation, turning the kinetic energy into heat. Since the energy cascade was introduced energy transfer in turbulent flows has remained an ongoing subject of investigation for decades (Kolmogorov 1941; Batchelor 1969; Godeferd & Cambon 1994; Smith & Waleffe 1999; Cimarelli *et al.* 2016). Energy transfer equations were originally derived using assumptions of homogeneity and isotropy for mathematical convenience, but despite numerous attempts to recreate such properties in the laboratory (Monin & Yaglom 1975), such properties are rarely found in real flows. Therefore, a number of studies have focused on understanding the effects of

† Email address for correspondence: anna.n.knutsen@ntnu.no

42 anisotropy, scale-dependence and inhomogeneity on energy transfer. The effect of mean
 43 flow gradients was considered by Deissler (1961, 1981), who through spectral analysis
 44 of general inhomogenous turbulence concluded that not only turbulent self-interactions,
 45 but also interactions between turbulent fluctuations and the mean flow are sources of
 46 inter-scale energy transfer, thus transferring energy from larger to smaller scales, or in
 47 the opposite direction. Further to this, Danaïla *et al.* (1999) suggested a modified version
 48 of Kolmogorov’s $-4/5^{th}$ law, which is derived for homogeneous, isotropic turbulence,
 49 by arguing that in many real and laboratory flows, the Reynolds number is not large
 50 enough to fully separate the small scales from the large scales, and that large scale
 51 and inhomogeneity effects would therefore affect the energy transfer. In this study an
 52 inhomogeneity term was added to the equation to make up for non-stationary moments of
 53 the velocity increments. Later studies by this group also considered a mean flow consisting
 54 of predominantly one component, which is varying only in one direction (Danaïla *et al.*
 55 2001, 2002), which would be the case in for example a channel flow. This allowed the
 56 effect of mean shear on the scaly-by-scale energy budget to also be included, resulting
 57 in a production term in the inter-scale energy equation. Hill (2002) derived from the
 58 incompressible Navier-Stokes equation, a formulation that can systematically assess all
 59 such contributions to the overall deviation from Kolmogorov’s $-4/5^{th}$ law, including
 60 inhomogeneity, anisotropy, unsteadiness, and large-scale effects. This evolution equation
 61 of the second order structure function is a fully generalised version of the Kármán
 62 Howarth equation (von Karman & Howarth 1938) which was originally derived for
 63 homogeneous, isotropic flows. The equation is sometimes referred to as the Kármán-
 64 Howarth-Monin-Hill (KMH) equation, and through its application, it is possible to
 65 describe the total flow of energy both in physical space and across spatial scales for any
 66 flow.

67 Recent studies have used this equation as a framework to investigate the transfer of
 68 energy in a range of different turbulent flows. Casciola *et al.* (2003) used a variant of
 69 the Kármán Howarth equation for homogeneous, anisotropic turbulence to study a ho-
 70 mogeneous shear flow using DNS. Similarly, a weak formulation of the Kármán Howarth
 71 Monin equation was used by Debue *et al.* (2018*b*) for investigating the effects of quasi-
 72 singularities or singularities in a von Kármán flow, and found that the extreme events of
 73 the instantaneous inter-scale energy transfer govern the intermittency corrections given
 74 in the refined similarity hypothesis (Kolmogorov 1962; Oboukhov 1962). Fully generalised
 75 versions of the Kármán Howarth equation have also been used in studies of anisotropic
 76 and inhomogeneous turbulence to study cascade behaviour in a rotating flow (Campagne
 77 *et al.* 2014), the relations between global and local energy transfers in a von Kármán
 78 flow (Kuzzay *et al.* 2015), in the near field region behind a grid (Gomes-Fernandes
 79 *et al.* 2015; Valente & Vassilicos 2015), and the planar wake generated by a square
 80 prism (Portela *et al.* 2017). A common feature in the majority of these previous studies
 81 is that mean flow contributions to the inter-scale energy budget are negligible, with
 82 the exception of the study by Portela *et al.* (2017), where gradients in the mean flow
 83 are present. In the absence of mean flow, contributions to the scale-to-scale transport
 84 often focus on the non-linear contribution, with all studies demonstrating some degree of
 85 inter-scale anisotropy. Furthermore, although the globally spherically averaged transfer
 86 of energy is in the forward cascade direction, defined such that energy is transported
 87 from larger to smaller scales, with the exception of Valente & Vassilicos (2015) these
 88 studies also all contain regions in scale space of locally inverse cascade behaviour, where
 89 energy is transferred from smaller to larger scales. Similarly Carter & Coletti (2018)
 90 investigated energy transfer in a jet-stirred turbulent flow, and observed anisotropy in
 91 the rate of energy transfer, despite well controlled flow homogeneity. Based on these recent

92 studies, it appears that the non-linear inter-scale energy transfer in different flows varies
93 significantly, and at present it is still uncertain how flow homogeneity and anisotropy in
94 different flows relates to the scale-space orientation of the energy transfer, and if inverse
95 cascade behaviour is omnipresent, or if the examples above represent exceptional cases.

96 In this work, we have performed a detailed study of the energy transfer of the flow
97 between two counter rotating disks or impellers, often referred to as a von Kármán
98 flow. The flow has been studied in a large number of analytical (Batchelor (1951);
99 Stewartson (1953); Zandbergen & Dijkstra (1987)), numerical (Mordant *et al.* 2004;
100 Kreuzahler *et al.* 2014; Nore *et al.* 2018) and experimental studies (Bonn *et al.* 1993;
101 Cadot *et al.* 1995; Voth *et al.* 1998; Ouellette *et al.* 2006; Bourgoïn *et al.* 2006; López-
102 Caballero & Burguete 2013; Lawson & Dawson 2015; Podvin & Dubrulle 2018; Debue
103 *et al.* 2018*b*; Lawson *et al.* 2019), and the setup is ideal for laboratory experiments as
104 high Reynolds numbers can be achieved in relatively small laboratory spaces. The mean
105 flow of the tank has been reported to be anisotropic and inhomogeneous (Porta *et al.*
106 2000) but the turbulent fluctuations at the very centre of the tank can be considered to
107 be locally homogeneous based on second order metrics (Lawson & Dawson 2014; Jucha
108 2014). Given the widespread use of this configuration in understanding the small scale
109 structure of turbulent flows, it is of significant interest to study the transfer of energy in
110 this apparatus.

111 The aim of this study is to use the full KMHM equation to investigate the inter-scale
112 energy budget and cascade behaviour in the well known axisymmetric homogeneous flow
113 generated by a von Kármán mixing tank. In particular we are interested in understanding:
114 Does the energy transfer in this flow share the same directional dependency or anisotropy
115 as other flows, and will this nominally statistically homogeneous axisymmetric flow also
116 exhibit regions of inverse cascade behaviour such as observed by Qu *et al.* (2017) in direct
117 numerical simulations of purely axisymmetric turbulence? Which processes are significant
118 to balance the energy budget at the various scales captured by the experiments? Given
119 the flow at the centre of von Kármán tanks have a very small mean component relative
120 to turbulent fluctuations, but with strong stationary gradients in all flow directions, how
121 significant is the linear inter-scale energy transfer?

122 A secondary objective of the current work is to leverage the recent development of
123 highly accurate and fully volumetric experimental methods (Lawson & Dawson 2015).
124 For many decades researchers had to rely on measurements made at a single-point
125 in the flow, and often only consider a single component of velocity (Pao 1965; Shen
126 & Warhaft 2002). More recently multi-component planar measurements have become
127 widely available (Campagne *et al.* 2014; Debue *et al.* 2018*b*). However, all such studies
128 require the use of symmetry assumptions (Gomes-Fernandes *et al.* 2015) to complete
129 their description of inherently three-dimensional quantities such as the dissipation rate;
130 a process which can be misleading (Thoroddsen 1995). In the present work we use
131 fully volumetric measurements, which allows us for the first time to experimentally
132 investigate energy transfer using the KMHM equations without the use of assumptions
133 or surrogates on which planar or point-wise measurements must rely (Carter & Coletti
134 2018; Gomes-Fernandes *et al.* 2015; Thiesset *et al.* 2011; Kuzzay *et al.* 2015). The current
135 investigation therefore employs both planar Stereoscopic and full volumetric Particle
136 Image Velocimetry (PIV), and the use of very large experimental data sets (200 000 and
137 40 000 samples from Scanning and Stereo PIV respectively) in order to converge the
138 higher order statistics.

139 Following an introduction of the notation and coordinate systems used in the paper
140 given in §2.1, a detailed description of the experimental methodology is presented in
141 §2.2, a brief flow characterisation is outlined in §2.3, and details of the method used

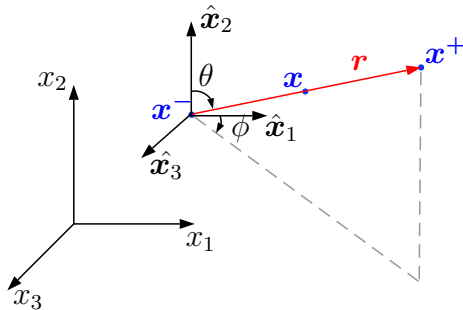


Figure 1: Schematic of the relative configuration of the considered points, vectors, and coordinate systems.

142 for calculating the inter-scale energy budget are described in §2.4. Following this, the
 143 distribution and transfer of energy is assessed in detail in §3. Here we begin by assessing
 144 the energy distribution and flux of energy in §3.1 and §3.2. The contribution of the
 145 non-linear transfer term to the energy budget is discussed in §3.3.1, before including the
 146 impact of the linear transfer term in §3.3.2. In §3.3.3 we focus on the way in which the
 147 energy budget is balanced, and take a closer look at local homogeneity in §3.4, before
 148 some conclusions are drawn.

149 2. Methodology

150 Data for this study were obtained using both volumetric Scanning PIV and planar
 151 Stereo PIV. Here, the notation, the experimental facility and methods are presented in
 152 addition to details on the vector field processing, a brief flow characterisation, and an
 153 introduction to the inter-scale energy budget.

154 2.1. Notation and coordinate system

155 This section aims to provide an overview of the notation in this work. In the present
 156 work the instantaneous velocity field $\mathbf{U}(\mathbf{x}, t)$ is Reynolds-decomposed into the time averaged,
 157 $\mathbf{U}(\mathbf{x})$, and fluctuating components, $\mathbf{u}(\mathbf{x}, t)$. Similarly, the instantaneous pressure
 158 field $\mathcal{P}(\mathbf{x}, t)$ is decomposed into a fluctuating, $p(\mathbf{x}, t)$, and a mean part, $P(\mathbf{x})$. We shall
 159 primarily be concerned with various averages of two-point measurements. The two points
 160 are denoted \mathbf{x}^+ and \mathbf{x}^- . We use superscripts $+$ and $-$ to denote quantities evaluated at
 161 \mathbf{x}^+ and \mathbf{x}^- . The points are centred at position at $\mathbf{x} = (\mathbf{x}^+ + \mathbf{x}^-)/2$ and are separated
 162 by a distance $r = |\mathbf{r}|$, where $\mathbf{r} = \mathbf{x}^+ - \mathbf{x}^-$. This configuration is illustrated in Figure 1.
 163 Cartesian coordinates are indexed $(1, 2, 3)$, are associated with unit vectors $\hat{\mathbf{x}}_1, \hat{\mathbf{x}}_2, \hat{\mathbf{x}}_3$,
 164 marked in Figure 2. Later, it shall be convenient to express separations \mathbf{r} in terms of
 165 polar coordinates (r, θ, ϕ) , where the polar direction is aligned with $\hat{\mathbf{x}}_2$ and the azimuth is
 166 measured from $\hat{\mathbf{x}}_1$ as shown in Figure 1. Similarly these are associated with unit vectors
 167 $\hat{\mathbf{r}}, \hat{\theta}$ and $\hat{\phi}$ and vector components are indicated with subscripts r, θ, ϕ .

We are interested in quantities, e.g. velocity increments $\delta\mathbf{u}(\mathbf{x}, \mathbf{r}, t) = \mathbf{u}(\mathbf{x}^+, t) - \mathbf{u}(\mathbf{x}^-, t)$, which are a function of both position \mathbf{x} in physical space and separation \mathbf{r} in scale space. Whenever a reference is made to the behaviour of a given quantity in the physical space, the \mathbf{x} dependence is meant, while the behaviour in scale space should be

understood in terms of \mathbf{r} dependence. The derivatives $\partial/\partial r_i$ and $\partial/\partial x_i$ are related by

$$\begin{aligned}\frac{\partial}{\partial x_i^+} &= \frac{\partial}{\partial r_i} + \frac{1}{2} \frac{\partial}{\partial x_i} & \frac{\partial}{\partial x_i^-} &= -\frac{\partial}{\partial r_i} + \frac{1}{2} \frac{\partial}{\partial x_i} \\ \frac{\partial}{\partial x_i} &= \frac{\partial}{\partial x_i^+} + \frac{\partial}{\partial x_i^-} & \frac{\partial}{\partial x_i} &= \frac{1}{2} \left(\frac{\partial}{\partial x_i^+} - \frac{\partial}{\partial x_i^-} \right)\end{aligned}\quad (2.1)$$

168 where summation over repeated indices is implied.

169 Three types of averaging operator are used: the time average, the spatial average and
170 the spherical average. We denote the time average of a signal $g(\mathbf{x}, \mathbf{r}, t)$ as \bar{g} and define

$$\bar{g}(\mathbf{x}, \mathbf{r}, T) = \frac{1}{T} \int_0^T g(\mathbf{x}, \mathbf{r}, t) dt. \quad (2.2)$$

171 This is experimentally approximated by an average over N_s samples. Since the number
172 of samples is large and acquired continuously over several days, we shall subsequently
173 drop the explicit dependence upon T in our notation. Spatial averages are denoted with
174 angled brackets $\langle g \rangle$ and defined

$$\langle g \rangle(\mathcal{A}, \mathbf{r}, t) = \frac{1}{|\mathcal{A}|} \int_{\mathcal{A}} g(\mathbf{x}, \mathbf{r}, t) d\mathbf{x} \quad (2.3)$$

175 where \mathcal{A} is the domain over which we measure g , in this case a region of approximately
176 homogeneous turbulence near the geometric center of the mixing tank. Additionally, $\partial\mathcal{A}$
177 is the boundary of \mathcal{A} . Since this region is fixed for the purposes of our experiment, we
178 shall subsequently drop the dependence upon \mathcal{A} from our notation. Finally, a spherical
179 average is denoted by $\langle g \rangle_\circ(\mathbf{x}, r, t)$ and is defined

$$\langle g \rangle_\circ(\mathbf{x}, r, t) = \frac{1}{4\pi r^2} \iint_{|\mathbf{r}|=r} f(\mathbf{x}, \mathbf{r}, t) dS_{\mathbf{r}} \quad (2.4)$$

180 and can be interpreted as the average of g over the surface of a sphere $|\mathbf{r}| = r$. The
181 spherical average operation requires 3D data, and for the Scanning PIV data, the
182 spherical average of the various terms are calculated directly. For the Stereo PIV data,
183 only data in a plane is available, and thus statistical axisymmetry is invoked to estimate
184 spherical averages.

185 2.2. Experimental setup

186 The full experimental setup used in this study consists of a von Kármán mixing tank,
187 a laser with an optical setup to guide the laser beam, and a pair of high speed cameras.
188 Figure 2(a) shows an overview image of the setup used for the Scanning PIV experiment.
189 The setup is the same as described by Lawson *et al.* (2019), but is presented here in more
190 detail.

191 The mixing tank, illustrated in figure 2(b), consists of a stainless steel cylinder with a
192 height of 58 cm and diameter of 48 cm, with two counter rotating impellers of diameter 25
193 cm, located in the top and bottom of the tank. The impellers have 8 baffled vanes of height
194 5 cm to increase the production of turbulence. The rotational speed of the impellers is
195 maintained at 0.2 Hz, which results in constant energy injection at the largest flow scale.
196 The cylinder is closed by two cooling plates which maintain a fixed water temperature
197 of 21.2°C, resulting in a kinematic viscosity $\nu = 0.975 \text{ mm}^2/\text{s}$. Between the impellers
198 and the cylindrical wall, eight static baffle plates are placed to suppress the large-scale
199 rotational motion that would otherwise occur, and to further increase the production of
200 turbulence. The measurement volumes from the Stereo and Scanning PIV experiments

are marked schematically in green in figure 2(b), where the small square illustrates the volumetric measurements. The measurements are made at the geometric centre of the tank, where the mean flow velocity is vanishing. The origin of the coordinates system (x_1, x_2, x_3) is also located in the geometric centre of the tank, while the axial direction coincides with \hat{x}_3 .

The laser beam passes through an optical setup consisting of two guiding mirrors, a (dynAXIS XS, Scanlab GmbH) galvanometer, followed by sheet forming optics, before passing through the measurement volume. A beam dump minimises back scattered light into the tank. For the Stereo PIV, the galvanometer was exchanged with a regular guiding mirror. For both experiments the laser light was used to illuminate the flow through light scattered from 6 μm diameter polymethyl methacrylate (PMMA) microspheres with specific gravity 1.22, which act as passive flow tracers (Stokes number of $St = 6 \times 10^{-5}$).

Two Phantom v640, 4 megapixel cameras were used for both the Stereo and Scanning PIV experiments. The full image of 2560×1600 pixels was used for the Stereo PIV measurements, while a smaller section of the camera sensor of 512×512 pixels was used in the Scanning PIV experiments due to limitations in the data uploading time.

With the exception of the optics, the setup for the two experiments were identical. An overview of the experimental parameters is given in Table 1. The Taylor microscale is estimated using the following relation, which is derived for isotropic flows:

$$\lambda^2 = \frac{15\nu\langle u_{rms} \rangle^2}{\langle \epsilon \rangle} \quad (2.5)$$

where $\langle u_{rms} \rangle$ is the spatial average of the RMS fluctuating velocity $u_{rms}(\mathbf{x}) = \sqrt{\frac{1}{3}u_i(\mathbf{x}, t)u_i(\mathbf{x}, t)}$, and $\epsilon(\mathbf{x}) = \nu \frac{\partial u_i(\mathbf{x}, t)}{\partial x_j} \frac{\partial u_i(\mathbf{x}, t)}{\partial x_j}$ represents dissipation of kinetic energy of turbulence. It is important to note that ϵ , as defined here, is the so called pseudo-dissipation. This is in opposition to the true dissipation, $\epsilon_{true} = 2\nu \overline{s_{ij}s_{ij}}$, where $s_{ij} = \frac{1}{2} \left(\frac{\partial u_i}{\partial x_j} + \frac{\partial u_j}{\partial x_i} \right)$. The difference between the two is usually small, and thus often neglected for the sake of the equations simplicity (Pope 2005). In the present work we are consequently using ϵ , and refer to it as dissipation (except for Appendix B, where ϵ_{true} is utilized). The longitudinal integral length scale, L_{LL} , is estimated using equation 2.6 applying the procedure described in Jong *et al.* (2009) (the spatial averaging is applied because the involved statistics are homogeneous to a large extent, as has been confirmed in auxiliary checks).

$$L_{LL} = \int_0^\infty \left\langle \frac{R_{LL}(\mathbf{x}, r)}{R_{LL}(\mathbf{x}, 0)} \right\rangle dr \approx \int_0^{r_{max}} \left\langle \frac{R_{LL}(\mathbf{x}, r)}{R_{LL}(\mathbf{x}, 0)} \right\rangle dr + \frac{A}{B} e^{-Br_{max}} \quad (2.6)$$

where $R_{LL}(\mathbf{x}, r)$ is the longitudinal autocorrelation function:

$$R_{LL}(\mathbf{x}, r) = \int_{|\mathbf{r}|=r} \frac{r_i r_j}{4\pi r^4} \overline{u_i(\mathbf{x} - \mathbf{r}/2, t) u_j(\mathbf{x} + \mathbf{r}/2, t)} dS \quad (2.7)$$

The definition of L_{LL} given by equation 2.6 involves integration from $r = 0$ to $r = \infty$, and thus, as the FoV is of finite size, an extrapolation of $\langle R_{LL}(\mathbf{x}, r) \rangle$ is required to approximate L_{LL} . Towards this purpose, an exponential decay of the form Ae^{-Br} is least-square fitted into the resolved tails of $\langle R_{LL} \rangle$. Further, we integrate $\langle R_{LL}(\mathbf{x}, r) \rangle$ up to its resolved limit r_{max} , and past that point we integrate the fit. The resultant relative contribution of the extrapolated part of $\langle R_{LL}(\mathbf{x}, r) \rangle$ in L_{LL} is 25.2%. The resulting value of $L_{LL} = 180.4\eta$, and is comparable to the value of L_{LL} estimated by Jucha *et al.* (2014)

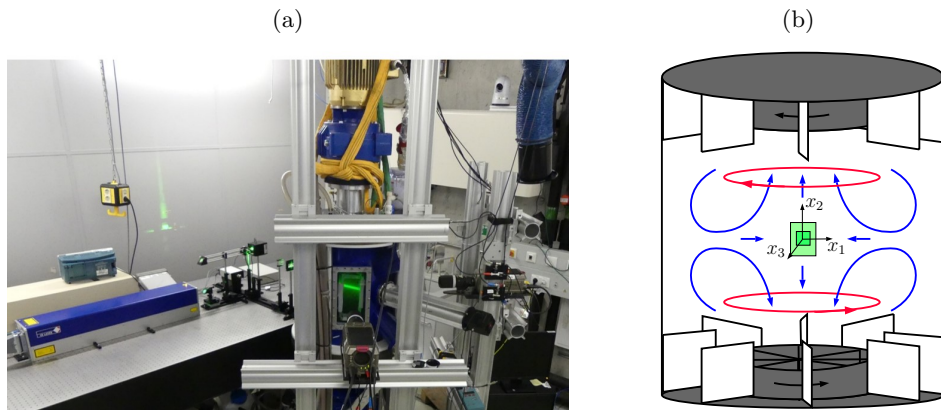


Figure 2: (a) Experimental setup with laser, optical configuration, flow facility and cameras. (b) Schematic of flow facility, with decomposition of the mean flow between the two counter rotating impellers: shear layer (—) and recirculation due to Ekman pumping (—). The two measurement volumes are marked in green, and the coordinate system (x_1, x_2, x_3) are given.

Parameter	Symbol	Value	Unit
Impeller rotation frequency	f	0.2	Hz
Impeller diameter	D	0.25	m
RMS velocity fluctuations	$\langle u_{rms} \rangle$	33.6	mm/s
Reynolds number	Re_λ	199	-
Mean dissipation rate	$\langle \epsilon \rangle$	492	mm^2/s^2
Kolmogorov timescale	τ	44.6	ms
Kolmogorov lengthscale	η	209	μm
Integral lengthscale	L_{LL}/η	180.4	-
Taylor microscale	λ/η	27.8	-
Kinematic viscosity	ν	0.975	mm^2/s
Density	ρ	1000	kg/m^3

Table 1: Flow parameters and calculated length and time scales.

239 in the same experimental facility. The Kolmogorov length and timescales are calculated
 240 as $\eta = (\nu^3/\langle \epsilon \rangle)^{1/4}$ and $\tau = (\nu/\langle \epsilon \rangle)^{1/2}$ respectively, and $Re_\lambda = \lambda \langle u_{rms} \rangle / \nu$.

241 2.2.1. Measurement techniques

242 Measurements were performed in a von Kármán mixing tank using both Stereoscopic
 243 PIV and Scanning PIV. The spatial resolution (window sizing) of the Scanning and Stereo
 244 PIV measurements are 3.06η and 2.04η respectively, resulting in a vector spacing of 0.76η
 245 and 1.16η . The sample sizes are 200 000 and 40 000 samples for the Scanning and Stereo
 246 PIV, sampled with a minimum spacing of respectively 2 and 4.5 large eddy turnover
 247 times, ensuring statistically independent measurements. Due to technical constraints,
 248 the measurement volume for the Scanning PIV is limited to $42\eta \times 42\eta \times 42\eta$. The Stereo
 249 PIV measurement covers a larger FoV ($154\eta \times 199\eta$), and therefore contributes to an
 250 understanding of the larger length scales of the flow.

251 The Stereoscopic PIV data was calibrated and processed using DaVis 8.3, to give 2D3C
 252 velocity fields. The processing involved the application of a multi-pass cross-correlation

algorithm with window deformation, and vector validation through application of the RMS criteria over local flow regions. The tomographic Scanning PIV algorithm described in Lawson & Dawson (2015) was employed to post-process the volumetric data. In short, the method consists of a laser sheet being traversed (scanned) across a measurement volume at a rate of 250Hz, while two high speed cameras capture particle images of each illumination. 54 images were captured per scan, and intensity volumes are reconstructed based on the particle images using a MART algorithm. The reconstructed volumes are then cross correlated to obtain vector fields of velocity. Similarly an in-house multi-pass algorithm with window deformation was used for the cross-correlation, and a correction is applied to correct for the finite sheet speed effects. For each sample, five scans were performed, giving five reconstructed particle volumes and four velocity fields, providing access to acceleration information. A divergence correction is applied to the velocity fields (Wang *et al.* 2017), and a Lagrangian filter similar to Novara & Scarano (2013) is then used on the velocity fields to increase the measurement accuracy. In the procedure, artificial tracers inserted to the calculated flow field are tracked backwards and forwards in time, then a second-order polynomial is fitted to these trajectories, where the linear and quadratic terms yield the velocity and the Lagrangian acceleration respectively. As a result, the truncation error and the random error due to the particle positions is reduced. The Lagrangian acceleration fields, $\frac{Du_i}{Dt} = \frac{\partial u_i}{\partial t} + u_j \frac{\partial u_i}{\partial x_j}$, are used to resolve pressure fields using a similar procedure as in Lawson & Dawson (2015). The incompressible Navier Stokes equation is rearranged to solve for the pressure gradient, $\frac{\nabla p}{\rho} = -\frac{Du_i}{Dt} + \nu \nabla^2 u_i$, and when discretized make up an over-determined set of linear equations, which is solved using a least-square fit. However, the artificially inserted particles on the edges of the volume might leave the FoV when tracked in time, and the material derivative in these point will be lost. As a solution to this, the Poisson equation, $\frac{\nabla^2 p}{\rho} = -\frac{\partial^2}{\partial x_i \partial x_j} (u_i u_j)$, is included to the set of linear equations. It should be noted that whenever possible fourth order central differences are used to estimate first order derivatives, and fifth order central differences are used for second order derivatives.

The volumetric method relies on accurate knowledge of the laser sheet position. The laser sheet position is first calibrated manually. A calibration plate is placed in the measurement volume at various depth positions, then images of the laser sheet itself are acquired while the sheet is traversed across the calibration plate. From these images, laser sheet parameters such as sheet width, spacing, position and orientation are calculated (see Lawson & Dawson (2014) for more details). In addition to this manual calibration, the laser sheet self-calibration method described by Knutsen *et al.* (2017) is performed to increase the accuracy of the calibration. This self-calibration is also performed during the experiment to maintain an accurate calibration over long acquisition periods (the data was collected continuously for 12 days), and to be able to detect and correct for potential galvanometer drift.

The Scanning PIV technique allows for seeding densities high enough to achieve spatially fully resolved volumetric measurements of the flow for the given Reynolds number, $Re_\lambda = 199$, which in turn allows us to directly calculate the local dissipation rate, for a flow which is expected to be fully developed (and exhibit an inertial subrange) according to the scaling presented by Dimotakis (2005). The large number of volumetric samples taken, combined with the high spatial resolution of the measurements provide well converged statistics of the complete volumetric and time dependent flow field without the use of any assumptions. A detailed list of the experimental parameters for the two measurement methods is presented in table 2.

An attempt to evaluate the uncertainty of the datasets has been made through an

Parameter	Stereo PIV	Scanning PIV
Region of interest	$140\eta \times 180\eta$	$42\eta \times 42\eta \times 42\eta$
PIV window size	2.4η	3.06η
PIV Inter-frame time [ms]	4	1.5
Sheet width	7.18η	5.26η
Ratio of sheet width to sheet spacing	-	3.86
Complete volumetric scans per sample	-	5
Vector spacing	1.16η	0.76η
Number of samples, N_s	40 000	200 000

Table 2: Experimental parameters for both Stereo and Scanning PIV measurements.

302 evaluation of how well the volumetric data obeys the divergence free criteria, and through
303 an estimate of the random measurement error through the correlation function. In
304 addition, where possible an effort has been made to put confidence intervals on certain
305 quantities. See Appendix A for more detailed information and results of the evaluation.

306 2.3. Flow characterisation

307 The two experimental data sets were taken in the same tank, under the same condi-
308 tions, but with different measurement techniques. It is therefore useful to classify the
309 similarities and differences between these two data sets, in addition to giving a general
310 characterisation of the flow in this von Kármán mixing tank. This comparison and a more
311 detailed flow characterisation is presented in Appendix B. For further flow characteristics,
312 in addition to a comparison with DNS data, see Lawson *et al.* (2019), which is based on
313 the same Scanning PIV dataset.

314 2.3.1. Mean velocity distribution

315 The mean flow can be viewed as a superposition of the two flow modes illustrated in
316 figure 2(b). The mean flow field calculated from the Stereo PIV data is shown in figure
317 3. Contours of normalized velocity magnitude, $|\mathbf{U}|/\langle u_{rms} \rangle$, show that the mean flow in
318 the centre of the tank is of an order of magnitude smaller than the mean fluctuations.
319 The two flow modes resulting in the mean flow are: first a rotating motion, which rotates
320 in opposite directions at the top and bottom of the tank, creating a shear layer in the
321 mid plane between the two impellers (Ravelet *et al.* 2004; Monchaux *et al.* 2006; Cortet
322 *et al.* 2009); and second a centrifugal pumping mode, which results in a straining of the
323 flow at the center of the tank.

324 The combination of the flow modes results in a stagnation point which occurs approxi-
325 mately at the geometric center of the tank. The stagnation point in the $x_1 - x_2$ plane for
326 the Stereo PIV data is calculated to be at $(x_{1,s}, x_{2,s}) = (5.22\eta, -0.1\eta)$, while the velocity
327 in the center of the measurement volume, $(x_1, x_2) = (0, 0)$, is $(U_1, U_2, U_3) = (1.7\%, 0.6\%,$
328 $4.3\%)$ of $\langle u_{rms} \rangle$. Characteristic for a von Kármán flow, strong gradients are present in
329 all components of the mean flow, with the highest gradient observed in the x_2 -direction.

330 2.4. Calculation of the inter-scale energy budget

331 The final part of this section is used to present the KMH equation, which governs the
332 evolution of the trace of the second order structure function $\delta q^2(\mathbf{x}, \mathbf{r}) \equiv \delta q^2(\mathbf{x}, \mathbf{r}, t) =$
333 $\delta u_i(\mathbf{x}, \mathbf{r}, t)\delta u_i(\mathbf{x}, \mathbf{r}, t)$. The KMH equation is given by eq. 2.8, where for the sake of
334 brevity we do not present the explicit functional dependency of the particular terms.

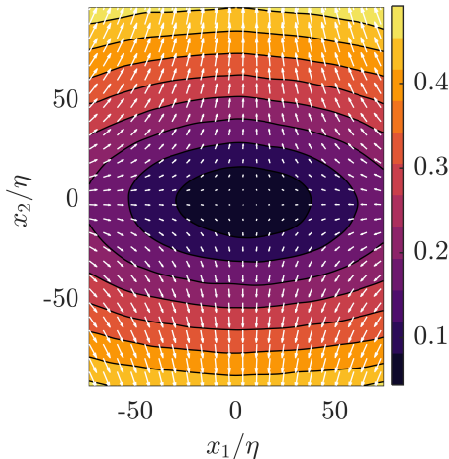


Figure 3: Mean flow from the Stereo PIV data. Contours represent the magnitude of the mean flow normalized by the mean fluctuations, $|\mathbf{U}|/\langle u_{rms} \rangle$, while the velocity vectors are showing the mean flow in the $x_1 - x_2$ plane. Every sixth vector is plotted.

$$\begin{aligned}
 & \frac{\partial \overline{\delta q^2}}{\partial t} + \frac{\partial}{\partial x_i} \left(\frac{U_i^+ + U_i^-}{2} \overline{\delta q^2} \right) + \frac{\partial}{\partial r_i} \overline{\delta u_i \delta q^2} + \frac{\partial}{\partial r_i} \overline{\delta U_i \delta q^2} = \\
 & - 2 \overline{\delta u_i \delta u_j} \frac{\partial}{\partial r_i} \overline{\delta U_j} - \overline{(u_i^+ + u_i^-) \delta u_j} \frac{\partial}{\partial x_i} \overline{\delta U_j} - \frac{\partial}{\partial x_i} \left(\frac{u_i^+ + u_i^-}{2} \overline{\delta q^2} \right) \\
 & - \frac{2}{\rho} \frac{\partial}{\partial x_i} \overline{\delta u_i \delta p} + \frac{\nu}{2} \frac{\partial^2}{\partial x_i \partial x_i} \overline{\delta q^2} + 2\nu \frac{\partial^2}{\partial r_i \partial r_i} \overline{\delta q^2} - 4\nu \left(\frac{\partial \overline{\delta u_j}}{\partial x_i} \frac{\partial \overline{\delta u_j}}{\partial x_i} + 4 \frac{\partial \overline{\delta u_j}}{\partial r_i} \frac{\partial \overline{\delta u_j}}{\partial r_i} \right) \quad (2.8)
 \end{aligned}$$

335 The integral of $\overline{\delta q^2}(\mathbf{x}, \mathbf{r})$ over a sphere of a specified radius $r = |\mathbf{r}|$ can be intuitively
 336 understood as 1/4 of the energy accumulated at the scales equal to and smaller than
 337 r (Davidson 2004). This becomes more apparent when $\overline{\delta q^2}$ is expressed with a Fourier
 338 integral, where $\mathbf{u}(\mathbf{x}, t) = \iint \int_{-\infty}^{\infty} \hat{\mathbf{u}}(\boldsymbol{\kappa}, t) \exp(i\boldsymbol{\kappa} \cdot \mathbf{x}) d\boldsymbol{\kappa}$, which can be written as:

$$\overline{\delta q^2}(\mathbf{r}) = 4 \iiint \int_{-\infty}^{\infty} \Psi(\boldsymbol{\kappa}, \mathbf{r}) \hat{E}(\boldsymbol{\kappa}) d\boldsymbol{\kappa} \quad (2.9)$$

339 where $\boldsymbol{\kappa}$ is the wavevector and summation goes over all Fourier modes, \hat{E} is the energy
 340 associated with $\boldsymbol{\kappa}$ and $\Psi = 1 - \cos(\boldsymbol{\kappa} \cdot \mathbf{r})$ can be looked upon as a filter which is weighing
 341 the wavenumbers which contribute to $\overline{\delta q^2}(\mathbf{x}, \mathbf{r})$.

342 Eq. 2.8 does not take into account any assumption of homogeneity or isotropy of the
 343 flow and thus considers both inter-space and inter-scale transfers of $\overline{\delta q^2}$.

344 Statistics of the studied flow are homogeneous, to a large degree, within the FoV (this
 345 was verified for all the particular terms of eq. 2.8). Therefore, in order to reduce the
 346 amount of data as well as for smoothing of our statistics, we shall consider the space-
 347 averaged version of eq. 2.8 in all further analysis (note that eq. 2.8 is valid everywhere
 348 in the flow field, and thus its space-average stays valid as well). The averaging is over
 349 the extent of the FoV. Using the same approach as Portela *et al.* (2017) and Gomes-
 350 Fernandes *et al.* (2015), the following terms of the space-averaged KMH equation are
 351 identified:

$$A_t = -A - \Pi - \Pi_U + \mathcal{P} + T_u + T_p + D_x + D_r - \epsilon_r \quad (2.10)$$

and the following meaning can be assigned to them ($\partial\mathcal{A}$ and \mathbf{n} designates the boundary of the FoV and its normal vector respectively):

$$A_t = A_t(\mathbf{r}, \mathcal{A}, T) = \frac{1}{4} \left\langle \frac{\partial}{\partial t} \overline{\delta q^2(\mathbf{x}, \mathbf{r}, t)} \right\rangle = \frac{1}{4} \frac{\partial}{\partial t} \left\langle \overline{\delta q^2(\mathbf{x}, \mathbf{r}, t)} \right\rangle$$

the spatially averaged unsteady term describes the rate of change in time of the kinetic energy $\frac{1}{4} \langle \overline{\delta q^2} \rangle$ at scale \mathbf{r} .

$$A = A(\mathbf{r}, \mathcal{A}, T) = \frac{1}{4} \left\langle \frac{\partial}{\partial x_i} \frac{U_i^+(\mathbf{x}, \mathbf{r}) + U_i^-(\mathbf{x}, \mathbf{r})}{2} \overline{\delta q^2(\mathbf{x}, \mathbf{r}, t)} \right\rangle = \frac{1}{8|\partial\mathcal{A}|} \iint_{\partial\mathcal{A}} (U_i^+(\mathbf{x}, \mathbf{r}) + U_i^-(\mathbf{x}, \mathbf{r})) \overline{\delta q^2(\mathbf{x}, \mathbf{r}, t)} n_i \, dS$$

the averaged advection of $\overline{\delta q^2}$ through the boundaries of the FoV.

$$\Pi = \Pi(\mathbf{r}, \mathcal{A}, T) = \frac{1}{4} \left\langle \frac{\partial}{\partial r_i} \overline{\delta u_i(\mathbf{x}, \mathbf{r}, t) \delta q^2(\mathbf{x}, \mathbf{r}, t)} \right\rangle = \frac{1}{4} \frac{\partial}{\partial r_i} \left\langle \overline{\delta u_i(\mathbf{x}, \mathbf{r}, t) \delta q^2(\mathbf{x}, \mathbf{r}, t)} \right\rangle$$

the spatially averaged non-linear inter-scale transfer of $\overline{\delta q^2}$ accounting for the effect of non-linear interactions of scales in redistributing $\overline{\delta q^2}$ in scale space.

$$\Pi_U = \Pi_U(\mathbf{r}, \mathcal{A}, T) = \frac{1}{4} \left\langle \frac{\partial}{\partial r_i} \overline{\delta U_i(\mathbf{x}, \mathbf{r}) \delta q^2(\mathbf{x}, \mathbf{r}, t)} \right\rangle = \frac{1}{4} \frac{\partial}{\partial r_i} \left\langle \overline{\delta U_i(\mathbf{x}, \mathbf{r}) \delta q^2(\mathbf{x}, \mathbf{r}, t)} \right\rangle$$

the spatially averaged linear equivalent of Π ; it accounts for inter-scale transfer of $\overline{\delta q^2}$ by the mean flow.

$$\mathcal{P} = \mathcal{P}(\mathbf{r}, \mathcal{A}, T)$$

$$= -\frac{1}{2} \left\langle \overline{\delta u_i(\mathbf{x}, \mathbf{r}, t) \delta u_j(\mathbf{x}, \mathbf{r}, t)} \frac{\partial}{\partial r_i} \overline{\delta U_j(\mathbf{x}, \mathbf{r})} \right\rangle - \left\langle \overline{(u_i^+(\mathbf{x}, \mathbf{r}, t) + u_i^-(\mathbf{x}, \mathbf{r}, t)) \delta u_j(\mathbf{x}, \mathbf{r}, t)} \frac{\partial \delta}{\partial x_i} U_j(\mathbf{x}, \mathbf{r}) \right\rangle$$

the spatially averaged production of $\overline{\delta q^2}$ by the mean flow gradients.

$$T_u = T_u(\mathbf{r}, \mathcal{A}, T) = -\frac{1}{8} \left\langle \frac{\partial}{\partial x_i} \overline{(u_i^+(\mathbf{x}, \mathbf{r}, t) + u_i^-(\mathbf{x}, \mathbf{r}, t)) \delta q^2(\mathbf{x}, \mathbf{r}, t)} \right\rangle$$

$$= \frac{1}{8|\partial\mathcal{A}|} \iint_{\partial\mathcal{A}} \overline{(u_i^+(\mathbf{x}, \mathbf{r}, t) + u_i^-(\mathbf{x}, \mathbf{r}, t)) \delta q^2(\mathbf{x}, \mathbf{r}, t)} n_i \, dS$$

the averaged transport of $\overline{\delta q^2}$ by the fluctuating velocity through the boundary of the FoV.

$$T_p = T_p(\mathbf{r}, \mathcal{A}, T) = -\frac{1}{2\rho} \left\langle \frac{\partial}{\partial x_i} \overline{\delta u_i(\mathbf{x}, \mathbf{r}, t) \delta p(\mathbf{x}, \mathbf{r}, t)} \right\rangle = \frac{1}{2\rho|\partial\mathcal{A}|} \iint_{\partial\mathcal{A}} \overline{\delta u_i(\mathbf{x}, \mathbf{r}, t) \delta p(\mathbf{x}, \mathbf{r}, t)} n_i \, dS$$

the flux of $\overline{\delta u_i \delta p}$ through the boundaries of the FoV.

$$D_x = D_x(\mathbf{r}, \mathcal{A}, T) = \frac{\nu}{8} \left\langle \frac{\partial^2}{\partial x_i \partial x_i} \overline{\delta q^2(\mathbf{x}, \mathbf{r}, t)} \right\rangle = \frac{\nu}{8|\partial\mathcal{A}|} \iint_{\partial\mathcal{A}} \frac{\partial}{\partial x_i} \overline{\delta q^2(\mathbf{x}, \mathbf{r}, t)} n_i \, dS$$

the averaged viscous diffusive flux of $\overline{\delta q^2}$ through the boundary of the FoV.

$$D_r = D_r(\mathbf{r}, \mathcal{A}, T) = \frac{\nu}{2} \left\langle \frac{\partial^2}{\partial r_i \partial r_i} \overline{\delta q^2(\mathbf{x}, \mathbf{r}, t)} \right\rangle = \frac{\nu}{2} \frac{\partial^2}{\partial r_i \partial r_i} \left\langle \overline{\delta q^2(\mathbf{x}, \mathbf{r}, t)} \right\rangle$$

the spatially averaged viscous diffusion of $\overline{\delta q^2}$ in scale-space.

$$\epsilon_r = \epsilon_r(\mathbf{r}, \mathcal{A}, T) = \frac{\nu}{2} \left(\left\langle \frac{\partial u_j^+(\mathbf{x}, \mathbf{r}, t)}{\partial x_i^+} \frac{\partial u_j^+(\mathbf{x}, \mathbf{r}, t)}{\partial x_i^+} \right\rangle + \left\langle \frac{\partial u_j^-(\mathbf{x}, \mathbf{r}, t)}{\partial x_i^-} \frac{\partial u_j^-(\mathbf{x}, \mathbf{r}, t)}{\partial x_i^-} \right\rangle \right) = \langle \epsilon \rangle$$

spatially averaged dissipation, which equivalent to $\langle \epsilon \rangle$.

381

The volumetric data permits direct assessment of all terms in the KMHM equation. However, as each term in the KMHM equation requires derivatives of averaged quantities in all flow directions, it is not possible to calculate them directly from the planar Stereo PIV measurements. Therefore, assumptions are required for this data set. Since the flow is assumed to be, on averaged, axisymmetric around the direction $\hat{\mathbf{x}}_2$, all the spatial derivatives in the circumferential direction (i.e. along $\hat{\mathbf{x}}_3$ in our present setup) of averaged

flow quantities are expected to vanish and thus are neglected. This assumption allows us to calculate different terms of the KHM equation, and since the volumetric data is measured under the same flow conditions in the same flow facility, it can be directly tested for the smaller length scales. Further, the unsteady term and the pressure terms are lacking from the Stereo PIV data. As the data in this study is collected over a large number of turnover times, it follows from the stationarity assumption that the contribution from the stationary term is expected to go to zero, however, it is a very intermittent quantity which is hard to converge, and its residual value can potentially be of non-negligible order.

3. Inter-scale kinetic energy budget

Having introduced the experimental setup and methods, we now describe both the distribution of energy across scales, and the transfer of energy in our flow of interest. Our aim is to report the flow behaviour, but also to compare this to other similar investigations. Therefore, we discuss both the scale space organisation of energy transfer, and the reduced spherically averaged transfer, as well as evaluating this against the classical cascade concept. We finally examine the total inter-scale transfer, and consider which physical phenomena help balance the inter-scale energy budget.

3.1. Second order structure functions and isotropy

The variation of the normalised combined second order structure function, $\langle \overline{\delta q^2} \rangle / \langle u_{rms} \rangle^2$, with separation distance is shown in figure 4 for the Stereo PIV measurements. Figure 4(a) shows the distribution of $\langle \overline{\delta q^2} \rangle$ in the $r_1 - r_2$ -plane, whereas line plots along different angles of θ in the $r_1 - r_2$ -plane is shown in 4(b). The non-circular contours in figure 4(a), and the fact that the lines for different values of θ in figure 4(b) show that energy is distributed anisotropically at all scales. The anisotropy is consistent with stronger longitudinal velocity correlations, and therefore lower kinetic energy variations along the symmetry axis of the flow at a given scale. The volumetric measurements from the Scanning PIV data (not shown) further shows that $\langle \overline{\delta q^2} \rangle$ is indifferent to rotation around the axis r_2 , which resembles the axisymmetry of single-point statistics around the axis of the tank, as discussed earlier.

In order to better understand this anisotropic distribution, let us consider a decomposition of $\langle \overline{\delta q^2} \rangle(\mathbf{r})$ into contributions from velocity components aligned with unit vectors of a spherical coordinate system (r, θ, ϕ) (see figure 1), namely $\langle \overline{\delta q^2} \rangle = \langle \overline{\delta u_i \delta u_j} \rangle \cdot (\hat{r}_i \hat{r}_j + \hat{\theta}_i \hat{\theta}_j + \hat{\phi}_i \hat{\phi}_j) = \langle \overline{\delta u_r^2} \rangle + \langle \overline{\delta u_\theta^2} \rangle + \langle \overline{\delta u_\phi^2} \rangle$.

Figure 5 shows the individual spherical components of $\langle \overline{\delta q^2} \rangle$. To show these over a large range of scales, again the functions are plotted in the $r_1 - r_2$ -plane from the Stereo PIV measurements. The figure demonstrates that the main contributions to $\langle \overline{\delta q^2} \rangle$ come from the out of plane component, $\langle \overline{\delta q_\phi^2} \rangle$, which is anticipated as this component is parallel to the shear plane and this is where the largest velocity fluctuations exist, and we therefore also expect higher velocity differences. The distribution of $\langle \overline{\delta q_\phi^2} \rangle$ also resembles that of $\langle \overline{\delta q^2} \rangle$, with elliptical contour lines stretched in the axial direction. Both the radial and polar parts of $\langle \overline{\delta q^2} \rangle$, shown in figure 5(a) and (b), are highly anisotropic especially at larger scales, as shown from the visibly non-spherical contour lines. From observing the shape of the contour lines, the terms become more isotropic at smaller scales. The contour lines of the radial part, $\langle \overline{\delta q_r^2} \rangle$, are also stretched in r_2 -direction in a similar way to the full term $\langle \overline{\delta q^2} \rangle$ and $\langle \overline{\delta q_\phi^2} \rangle$, resulting in lower values along the r_2 -direction than for the r_1 -direction. This is as expected, as the \mathbf{r} -vector is aligned with the shear plane along the

434 r_1 -axis, where there are higher fluctuations and thus lower correlations. The azimuthal
 435 term exhibits an opposite behaviour, where we observe slightly higher values along the
 436 diagonal, and stretched contours in r_1 -direction.

437 To further quantify the level of isotropy and how this varies with scale and for the
 438 different components, let us define a measure of isotropy of an arbitrary function $f(\mathbf{r})$
 439 at a given scale r designated as $\sigma_f(r)$:

$$\sigma_f(r) = \frac{1}{\langle f(\mathbf{r}) \rangle_\circ} \sqrt{\langle (f(\mathbf{r}) - \langle f(\mathbf{r}) \rangle_\circ)^2 \rangle_\circ} \quad (3.1)$$

440 Note that the above definitions is equivalent to considering the L_2 norm of coefficients
 441 in a spherical harmonics decomposition (Arad *et al.* 1999; Kurien *et al.* 2000).

442 If $\langle \delta q^2 \rangle$ was distributed isotropically, this parameter would take a constant value of
 443 zero. The results demonstrate that the standard deviation of the contour lines along
 444 constant $\langle \delta q^2 \rangle$ is never zero, and that deviations in $\langle \delta q^2 \rangle$ along a constant radius,
 445 representing the level of anisotropy, increase with separation distance until $r \approx 60\eta \approx$
 446 $0.33L_{LL}$, where the curve flattens out before it starts to slightly decrease at $r \approx 100\eta \approx$
 447 $0.55L_{LL}$. From $r = 60\eta$ to $r = 130\eta$, the value of $\sigma_{\langle \delta q^2 \rangle}$ is constant to within 10% of its
 448 maximum value. One would expect increasing anisotropy for larger scales, but studying
 449 figure 6, it is clear that also $\langle \delta q_\phi^2 \rangle$ shows the same tendency to plateau within the FoV.
 450 The plateau behaviour and the slight decrease in anisotropy of both $\langle \delta q^2 \rangle$ and $\langle \delta q_r^2 \rangle$ may
 451 be caused by the increasing importance of $\langle \delta q_\theta^2 \rangle$. From figure 5(b) it is clear that the
 452 contour lines of $\langle \delta q_\theta^2 \rangle$ are elongated in the r_1 -direction while the other two terms are
 453 elongated in the r_2 -direction, especially for larger values of r , and thus making the final
 454 term $\langle \delta q^2 \rangle$ more isotropic than its components, i.e. different RMS values for different
 455 velocity components.

456 Figure 6 shows that while the distribution of $\langle \delta q^2 \rangle$ is anisotropic at all scales, the
 457 level of anisotropy is highest for $r \approx 100\eta$. If the anisotropy is driven by the shear layer
 458 between the counter rotating fluid cells, it is expected to increase with distance from the
 459 axis of symmetry following the shear. However, the plateau in the level of anisotropy
 460 results from the balance between the increments of the different velocity components.
 461 The terms $\langle \delta q_r^2 \rangle$ and $\langle \delta q_\theta^2 \rangle$ are anisotropic even at very small scales, which is a result
 462 of the apparent anisotropy of single-point velocity statistics. However, there are initial
 463 decreases of anisotropy of both terms (with minima respectively at 7η and 10η), followed
 464 by the subsequent growths. This behaviour, although surprising, might be the result
 465 of specific relations between directional Taylor microscales, directional integral length
 466 scales, and variances of particular velocity components.

467 A more thorough investigation of $\langle \delta q_r^2 \rangle$ is motivated by the highly anisotropic distri-
 468 bution of the term. Figure 7 demonstrates the orientation dependency of $\langle \delta q^2 \rangle$ through
 469 a line plot in (a), where the value of the term is plotted at different values of polar
 470 coordinate θ , and in (b) where the full distribution of the term is shown. $\langle \delta q_r^2 \rangle$ is the
 471 longitudinal second order structure function, which for homogeneous isotropic turbulence
 472 is related to the dissipation rate through Kolmogorov's 2/3rds law:

$$\overline{\delta u_r^2}(\mathbf{r}) = C_2 \epsilon^{2/3} |\mathbf{r}|^{2/3} \quad (3.2)$$

473 where C_2 is a constant which is expected to be universal (Pope 2005). In the present
 474 study a value of $C_2 = 2.1$ is found from the spherical average of $\langle \delta u_r^2 \rangle_\circ(r)$, shown in the
 475 inset in figure 7(a), which is consistent with previous studies (Ni & Xia 2013).

476 Figure 7 shows the normalized $\langle \delta q_r^2 \rangle$, which is expected to have a constant value in the

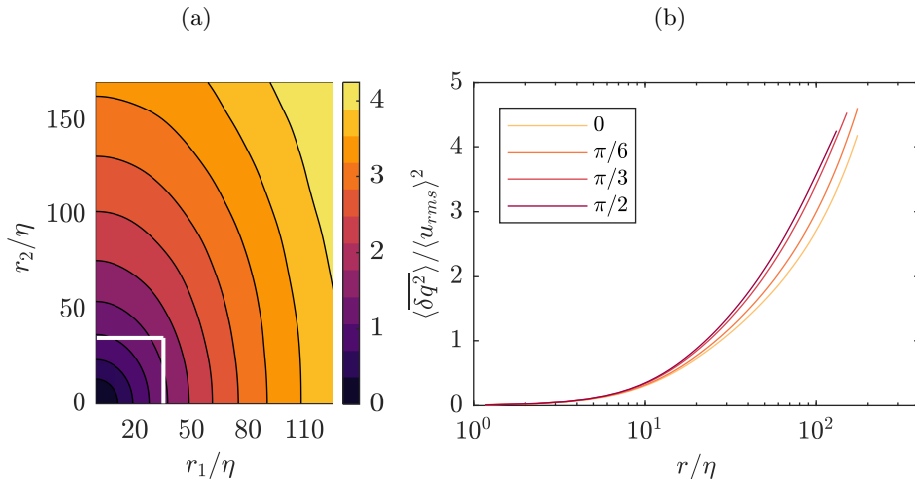


Figure 4: Distribution of $\langle \overline{\delta q^2} \rangle$ normalized by $\langle u_{rms} \rangle^2$ from Stereo PIV data normalized by $\langle u_{rms} \rangle$ from (a) the Stereo PIV data, and (b) the Scanning PIV data. The different isosurfaces in (b) Line plots of $\langle \overline{\delta q^2} \rangle$ for constant values of $\theta = [0, \pi/6, \pi/3, \pi/2]$.

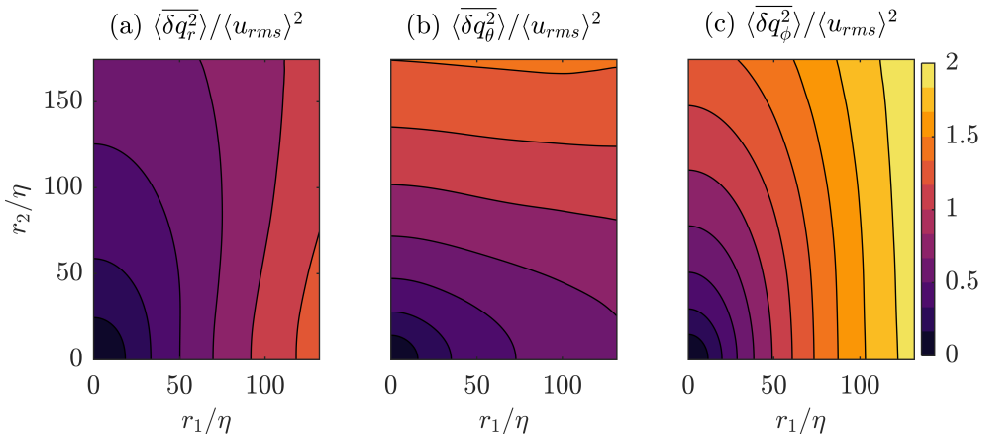
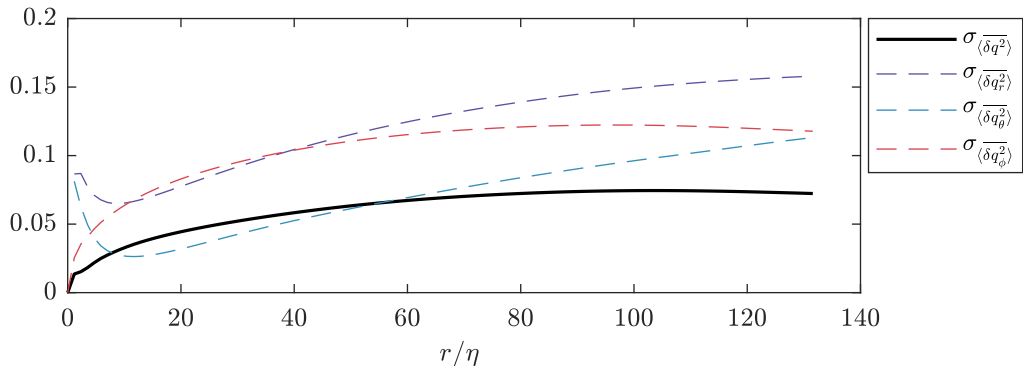
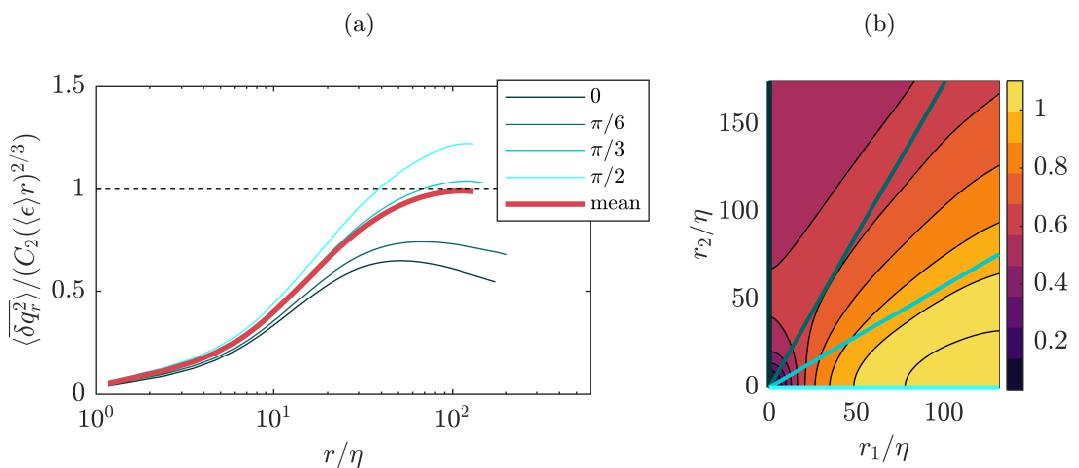


Figure 5: Spherical decomposition of $\langle \overline{\delta q^2} \rangle$ from Stereo PIV data normalized by $\langle u_{rms} \rangle^2$.

477 inertial range, and for most orientations, the term have reached a plateau. The plateau
 478 has, however, a different value for different orientations. This directional dependency
 479 indicates that, depending on along which orientation we calculate the second order
 480 longitudinal structure function, the resulting dissipation rate would vary significantly
 481 if a constant value of C_2 is used. This result is in contrast to the findings in Chang *et al.*
 482 (2012), where they study an anisotropic, zero shear flow, and conclude that C_2 shows no
 483 dependency on isotropy. This indicates that the mean flow gradients in the von Kármán
 484 flow cause the directional dependency of C_2 , which is consistent with the predictions in
 485 Lumley (1967), which are discussed in §3.4 in Biferale & Procaccia (2005). The term
 486 also levels off at different values for r , indicating that the onset of the inertial range is
 487 also dependent on orientation in scale space. This is consistent with the anisotropy we
 488 observe at small scales.


 Figure 6: Isotropy metric σ of $\langle\delta q^2\rangle$ and its spherical components.

 Figure 7: Orientational variation of $\langle\delta q_r^2\rangle$ normalized. (a) Along fixed values of θ , where the inset shows the spherical mean value. (b) Contour plot of $\langle\delta q_r^2\rangle / (C_2((\epsilon)r)^{2/3})$. Lines from (a) marked in (b).

3.2. Energy transfer and isotropy

489

490 After establishing the scale space distribution of energy, it is now of interest to examine
 491 both the magnitude and direction of energy transfer. This is presented through the flux
 492 of $\langle\delta q^2\rangle$ in scale space, $\langle\delta \mathbf{u} \delta q^2\rangle$, which is shown in figure 8(a) and (d) for the Stereo
 493 and Scanning PIV data respectively. While the discussion relates mainly to the planar
 494 data which covers a wider range of scales, good agreement is consistently observed at
 495 smaller scales for the volumetric data. Here the contours represent the flux magnitude,
 496 and the quiver arrows indicate the vector orientation which represents the scale space
 497 direction of the energy transfer. As separation distance increases so does the magnitude
 498 of the energy transfer, and therefore energy transfer takes place primarily at larger scales.
 499 There is, however, a significant level of anisotropy shown at all scales, with a non-uniform
 500 preference for transfer at horizontal and vertical scales, shown by the peak magnitude,
 501 which is observed at a scale space location of $(r_1/\eta, r_2/\eta) \approx (100, 150)$.

502 It is interesting to consider this distribution together with the direction of the energy
 503 transfer. The quiver arrows describe the redistribution of $\langle\delta q^2\rangle$ in scale space. A purely

504 radial vector distribution pointing towards the origin $(r_1, r_2) = (0, 0)$ would mean energy
 505 was being transferred directly from larger to smaller scales. This radial part of the energy
 506 flux is hereafter represented by $\langle \delta u_r \delta q^2 \rangle \equiv \langle \delta \mathbf{u} \delta q^2 \rangle \cdot \hat{\mathbf{r}}$. It is, however, clear that the
 507 orientation of the vectors are rarely purely radial. Whenever $|\langle \delta \mathbf{u} \delta q^2 \rangle|$ and $\langle \delta u_r \delta q^2 \rangle$
 508 are not the same, there is also a redistribution of $\langle \delta q^2 \rangle$ at the given scale r from one
 509 orientation to another, and energy is not purely transferred across scales.

510 The amount of scale to scale transfer and redistribution is indicated through the vectors
 511 in figure 8(a) and (e), and is made more explicit through the calculation of the angle
 512 between $\langle \delta \mathbf{u} \delta q^2 \rangle$ and the radial vector, \mathbf{r} , which is denoted, α , and plotted in figure 8(b)
 513 and (f). These figures show that along the horizontal and vertical axes, where $r_2 \ll \eta$ and
 514 $r_1 \ll \eta$ respectively, the angle $\alpha \approx 0^\circ$, and therefore the energy is only transferred down
 515 scale without redistribution. While the magnitude along the vertical axis is relatively
 516 small, the magnitude is more significant along the horizontal axis indicating a reasonable
 517 level of energy transfer along this path. Alternatively, away from the horizontal and
 518 vertical axes it appears that at the majority of scales, a combination of downscale energy
 519 transfer and redistribution within certain scales coexist, evidenced through non-zero
 520 values of α within a range of 0° to 60° . The positive distribution of the angle arises
 521 due to the combination of radial and horizontal components, meaning there is often a
 522 significant component of the flux pointing toward the symmetry axis. This implies energy
 523 is redistributed to structures which are orientated such that they result in higher velocity
 524 correlations in the vertical direction in comparison with the horizontal direction, before
 525 being transported down the scales. This redistribution of energy therefore mirrors the
 526 behaviour of the mean velocity field and may therefore be directly related to the axially
 527 straining of the flow field which exists at the centre of the flow.

528 To clarify this still further it is possible to isolate the down-scale transfer of energy from
 529 the total energy transfer. To this end figures 8(c) and (g) show the radial component of
 530 the third order structure function, $\langle \delta u_r \delta q^2 \rangle$, where the positive direction is defined away
 531 from the origin. For comparison, the tangential component, $\langle \delta u_\theta \delta q^2 \rangle \equiv \hat{\boldsymbol{\theta}} \cdot \langle \delta \mathbf{u} \delta q^2 \rangle$, is also
 532 included in figures 8(d) and (h). From the figures, it is clear that the radial component
 533 dominates the transfer. $\langle \delta u_r \delta q^2 \rangle$ shows a strong orientation dependence, which is very
 534 similar in terms of its distribution to the magnitude of $\langle \delta \mathbf{u} \delta q^2 \rangle$. Therefore, this shows
 535 that despite a certain amount of energy redistribution at some scales the majority of
 536 the energy is transferred down-scale. The characteristic non-spherical distribution of
 537 this down-scale transfer however shows that this transfer occurs anisotropically, with
 538 structures with higher velocity increments in the r_1 -orientation dominating the transfer.
 539 This preferential transfer of energy at different scale space orientations represents a
 540 departure from the straightforward concept of isotropic down-scale energy transfer. These
 541 distributions of energy transfer also show significant differences from those obtained in
 542 nominally isotropic cases (Lamriben *et al.* 2011; Carter & Coletti 2018), raising the
 543 possibility that the large scale flow continues to exert an influence even at small scales.

544 Despite the small magnitude of the mean flow relative to the turbulent fluctuations, it
 545 is also interesting to examine its role in the transfer of $\langle \delta q^2 \rangle$. Therefore, the magnitude
 546 of the flux of $\langle \delta q^2 \rangle$ in scale space by the mean flow, $|\langle \delta \mathbf{U} \delta q^2 \rangle|$, is shown in figure 9(a).
 547 The magnitude and orientation of the flux follow the mean flow distribution, increasing
 548 in magnitude with separation distance, r . However, perhaps surprisingly, the magnitude
 549 of this flux is of an order of magnitude larger than the flux of $\langle \delta \mathbf{u} \delta q^2 \rangle$ by the turbulent
 550 fluctuations. This is a result of the strong spatial mean flow gradients, and the mean
 551 stagnation flow pattern characteristic of this configuration, which result in significant

mean velocity differences for intermediate separation distances due to the inhomogeneity of the mean flow despite its relatively low magnitude.

In terms of directionality, the vector arrows are negative in the r_1 -direction indicating down-scale transport of energy along this axis, while they are positive in the r_2 -direction, resulting in a transfer of energy up the scales along this axis. This balance is made more explicit in figure 9(b), which shows the radial component of this term, $\langle \delta U_r \delta q^2 \rangle \equiv \langle \delta \mathbf{U} \delta q^2 \rangle \cdot \hat{\mathbf{r}}$. The positive and negatively signed regions indicate a net transfer of energy by the mean flow down-scale for angles $50^\circ < \theta < 90^\circ$, and up-scale for $0^\circ < \theta < 50^\circ$. Even excluding scale to scale redistribution, the magnitude of the energy transfer is still significantly larger than that of the turbulent fluctuations. Therefore, despite the small relative magnitude of the mean flow at the centre of a von Kármán tank, this dominates the scale to scale energy transfer. Therefore, in contrast to previous investigations in which the mean flow contribution is negligible (Campagne *et al.* 2014; Gomes-Fernandes *et al.* 2015; Valente & Vassilicos 2015; Carter & Coletti 2018), the role of the mean flow cannot be neglected in the present work and will be further examined in the following sections.

3.3. Application of the spherically averaged KMH equation

In order to understand the evolution of the energy distribution we now begin to examine the KMH equation. It is again an advantage to use both the planar data for the larger FoV, and the volumetric data both to be able to validate the planar data at small length scales, and to have direct access to all terms in the KMH equation without the use of assumptions. In order to determine which contributions play the most significant role in the inter-scale energy transfer in terms of magnitude we begin by analysing their spherical averages, which are shown in figure 10, with each term normalised by $\langle \epsilon \rangle$. 95% confidence intervals are calculated as described in Appendix A. The width of the confidence intervals increase with separation distance as expected, due to the reduction in available samples for higher separations. The greatest uncertainties were calculated for the Stereo PIV data and the Scanning PIV data, with a value of 5.8% of $\langle \epsilon \rangle$ for $\langle T_u \rangle_\circ$, and 4.6% of $\langle \epsilon \rangle$ for $\langle A_t \rangle_\circ$ respectively. This low level of uncertainty results from the extremely large size of the data sets.

Examining initially the planar data described in figure 10(a), up to intermediate scales ($r < 90\eta$) it is clear that the budget is dominated by non-linear transfer, $\langle \Pi \rangle_\circ$, and the viscous diffusion term, $\langle D_r \rangle_\circ$, with the other terms only becoming significant at larger scales. As the viscous diffusion terms only contribute at very low separation distances, where the viscous forces are significant ($r/\eta \ll 25$), within the range $6\eta < r < 90\eta$ the energy transfer is therefore defined primarily by the non-linear term. This balance is confirmed by the volumetric measurements shown in figure 10(b), which show a very similar distribution of terms over the restricted range of scales available to this technique. Given that the residual dissipation rate $\epsilon_{res} = A_t + A + \Pi + \Pi_U - \mathcal{P} - T_u - T_p - D_x - D_r$ normalised with the directly evaluated dissipation, i.e. $\epsilon_{res}/\langle \epsilon \rangle$, should have a constant value of 1, the volumetric measurements demonstrate the energy transfer budget is well captured, with a maximum residual deviation of 2.9%. Therefore, it can be stated that $\epsilon_{res}/\langle \epsilon \rangle = 1$ within the uncertainty of the measurements. This is an important test that is only possible to make with the volumetric time resolved measurements, which allow the unsteady, A_t , and pressure, T_p , terms to be directly quantified.

The instantaneous value of the non-linear inter-scale energy transfer, $\frac{\partial}{\partial r_i} \delta u_i \delta q^2$ fluctuates dramatically, from highly positive to highly negative values, in accordance with the results from Debue *et al.* (2018b), and it is only when considering its mean value over

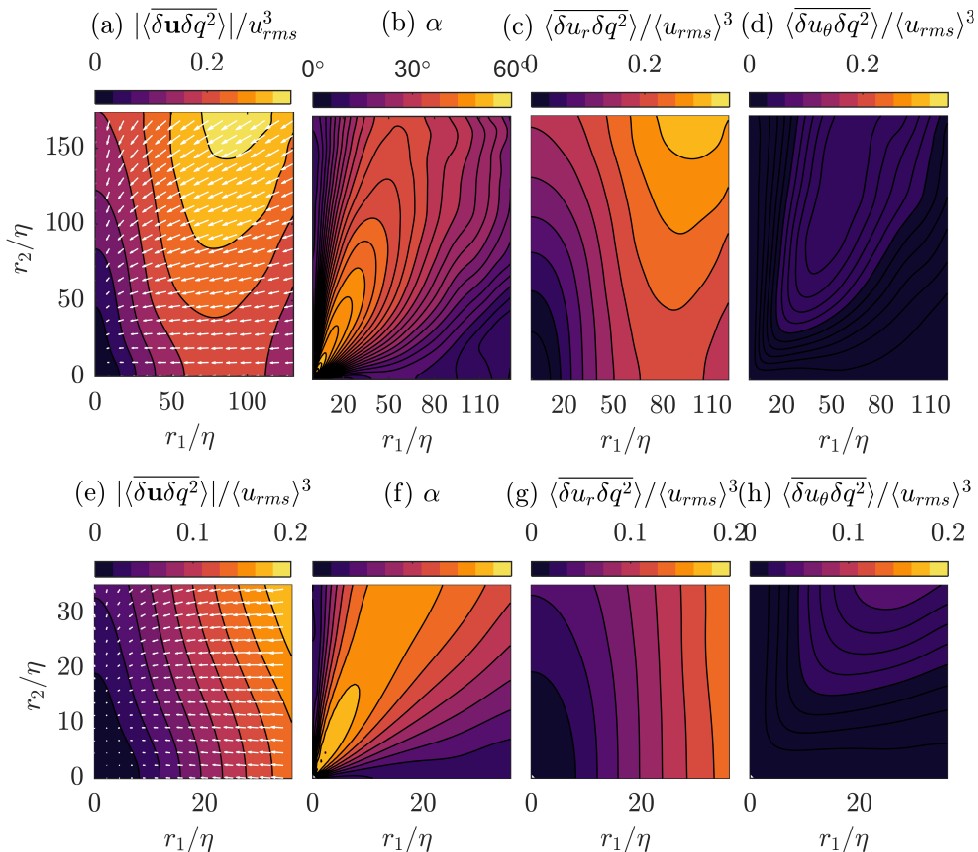


Figure 8: (a,e) Distribution of magnitude of $\langle \delta \mathbf{u} \delta q^2 \rangle$ with quiver arrows indicating the orientation of the vector $\langle \delta \mathbf{u} \delta q^2 \rangle$. For better visibility only every eight vector is plotted. (b,f) Deviation angle, the angle between radial vector \mathbf{r} pointing towards the origin and $\langle \delta \mathbf{u} \delta q^2 \rangle$. (c,g) Radial part of third order structure function, $\langle \delta u_r \delta q^2 \rangle$ (positive direction is set parallel to \mathbf{r} .), (d,h) Tangential part of third order structure function, $\langle \delta u_\theta \delta q^2 \rangle$. (a-d) from Stereo PIV data, while (e-h) from Scanning PIV data.

time that $\frac{\partial}{\partial r_i} \overline{\delta u_i \delta q^2}$ is positive. It is of particular interest to consider the magnitude of $\langle \Pi \rangle_\circ$ in terms of Kolmogorov's hypothesis of local equilibrium, where it is assumed that this term should equal the dissipation rate in the inertial range of scales, $\Pi = -\epsilon$. From the planar data Π is not reaching a plateau, but instead increases rapidly at small scales before reaching a maximum value of $-0.89\langle \epsilon \rangle$ at a scale $\approx \lambda$, and then decreases slowly with increasing length scale. Therefore, the prediction $\langle \Pi \rangle_\circ \approx -\langle \epsilon \rangle$ is quite reasonable around $r = \lambda$. In this case the underlying reason for the success of this prediction then is the small magnitude of the remaining spherically averaged terms in the KMH equation, combined with the mixed sign of these which act to cancel each other out to some degree.

The terms A and T_u from the KMH equation represent transport of $\langle \delta q^2 \rangle$ in physical space by the mean flow and the fluctuations respectively. When integrated over all separations r , these terms can be compared with the findings of Marié & Daviaud (2004) who investigated the importance of the mean flow and the turbulent fluctuations in

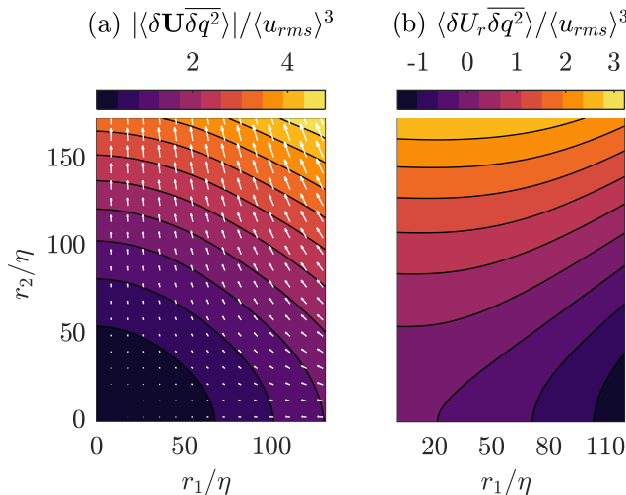


Figure 9: (a) Distribution of magnitude of $\langle \delta \mathbf{U} \overline{\delta q^2} \rangle$ with quiver arrows indicating the orientation of the vector $\langle \delta \mathbf{U} \overline{\delta q^2} \rangle$ normalised by $\langle u_{rms} \rangle^3$. For better visibility only every eighth vector is plotted. (b) Distribution of radial flux $\langle \delta q^2 \rangle$ by mean flow, $\langle \delta \mathbf{U} \overline{\delta q^2} \rangle$.

613 the angular momentum budget in physical space in a von Kármán flow. From the current
 614 study, we see that $\langle A \rangle_o$ is zero for all separations both from the volumetric and the planar
 615 measurements, whereas $\langle T_u \rangle_o$ has a non-zero value, and will thus dominate the transfer
 616 of $\langle \delta q^2 \rangle$ in physical space. The significance of the mean flow and the fluctuations for
 617 the transport of $\langle \delta q^2 \rangle$ in the center of the tank is therefore comparable to the transport
 618 of momentum found in Marié & Daviaud (2004). Further, $\langle D_x \rangle_o$, which is negligible at
 619 all scales accessible in the current study, can be compared to the viscous term studied
 620 in Marié & Daviaud (2004) (equation 3), which was reported to have a small overall
 621 contribution.

622 It is also worth observing that the Taylor microscale appears to reasonably define
 623 the transition between viscous and inertial ranges based on the decreasing significance
 624 of $\langle D_r \rangle_o$ and the increasing significance of $\langle \Pi \rangle_o$, which is in agreement with Valente &
 625 Vassilicos (2015), where they prove that $\langle D_r \rangle_o$ is only significant at scales smaller than λ .
 626 This might, however, be a coincidence as this coincides with the conventional beginning
 627 of the inertial range at $r \approx 30\eta$ (Pope 2005). The behaviour of $\langle D_r \rangle_o$ has earlier been
 628 predicted (Dubrulle 2019) and shown (Debye *et al.* 2018b) to follow a scaling of $r^{-4/3}$,
 629 which is consistent with the results from the current study, shown in figure 11.

630 At larger length scales ($r > 90\eta$) the linear transfer, $\langle \Pi_U \rangle_o$, turbulent production,
 631 $\langle \mathcal{P} \rangle_o$, and turbulent transport, $\langle T_u \rangle_o$, all become increasingly significant, reaching the
 632 same order of magnitude as the non-linear transfer term. As the mean velocity gradients
 633 are uniform over extended spatial areas, the expected inertial range scaling of the second
 634 order structure function implies that $\langle \Pi_U \rangle_o$ scales as $r^{2/3}$, in contrast to r^0 , and this can
 635 explain why $\langle \Pi_U \rangle_o$ becomes important at larger scales. The pressure term, $\langle T_p \rangle_o$, also has
 636 a contribution to the overall budget which is negative and has an increasing magnitude
 637 with increased separation. At $r \approx 130\eta$, the spherical averaged production reaches a value
 638 of $\langle \mathcal{P} \rangle_o \approx 0.57\langle \epsilon \rangle$. The production of $\langle \delta q^2 \rangle$ is a result of flow anisotropy, acting through
 639 the tensors $\langle \overline{\delta u_i \delta u_j} \rangle$ and $\langle (u_i^+ + u_i^-) \delta u_j \rangle$. Had the flow been isotropic at these scales there
 640 would be no production in this region. As this is not the case, there is a contribution
 641 from the production term at all scales. The spherical averaged production, $\langle \mathcal{P} \rangle_o$, at a

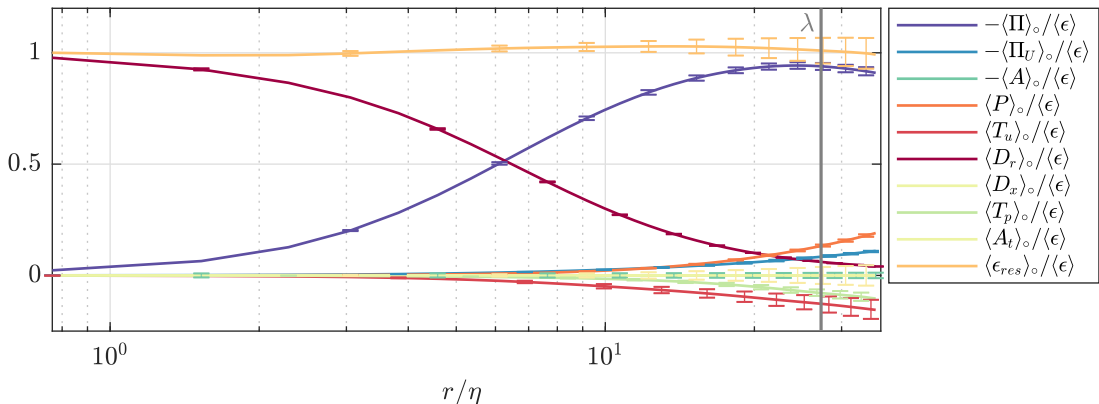
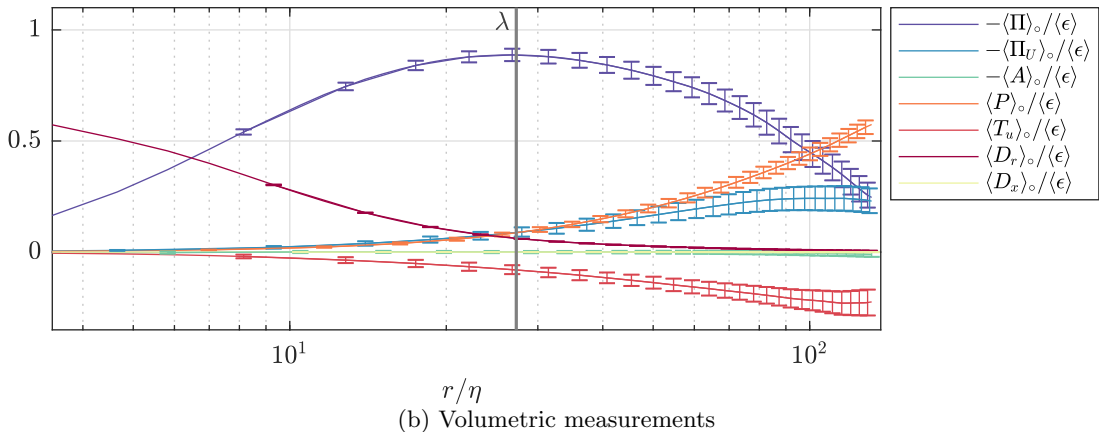


Figure 10: Spherical averaged terms of the KMH equation for the planar and volumetric measurements, where the subscript \circ indicates spherical mean values. The Taylor microscale λ is marked.

642 certain length scale r represents the total production at that length scale and smaller.
 643 Both data sets show that the production first increases parabolically until around 20η ,
 644 resulting in a linear derivative with respect to r , after which it has a linear growth, and
 645 a constant derivative, this is illustrated in figure 12, where the production term together
 646 with the parabolic and linear fits from both data sets are shown. The constant slope
 647 when $r > 20\eta$ indicates a constant production at these scales, while the parabolic shape
 648 at smaller separations indicates a linearly increasing production at larger length scales.
 649 As previously observed, the flow is more isotropic at the smallest scales resulting in
 650 lower production at these scales. Consideration of these terms in addition to the non-
 651 linear transfer and diffusion terms provides a more complete description of the energy
 652 budget over the range of scales examined in this spherically averaged sense. However, it
 653 is also interesting to examine the scale space distribution and hence the anisotropy of
 654 the significant terms in more detail, which is undertaken in the next two sections.

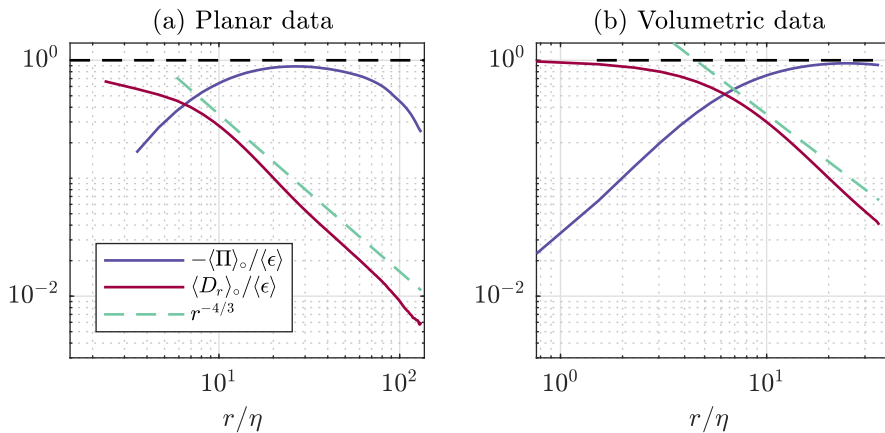


Figure 11: Spherical averages of the viscous term, $\langle D_r \rangle_\circ$, and the non-linear inter-scale transfer term, $\langle \Pi \rangle_\circ$ (a) from planar measurements, and (b) from volumetric measurements, showing a scaling of the of $\langle D_r \rangle_\circ$ in agreement with the predictions by Dubrulle (2019).

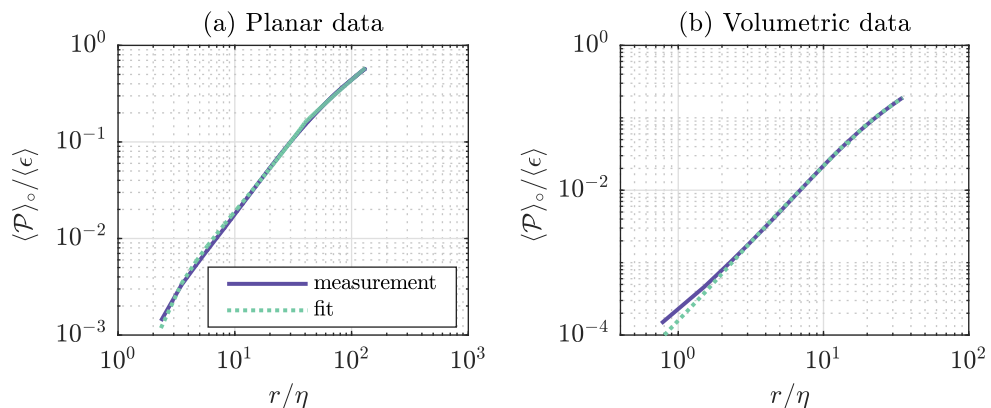


Figure 12: Measured and fitted spherically averaged values of the production term of KHM equation from (a) the planar data and (b) the volumetric PIV data.

655 3.3.1. Inter-scale transfer and the energy cascade

656 In this section we examine the scale space distribution of the divergence of the inter-
 657 scale energy flux, Π , in order to evaluate in more detail the mechanisms by which energy
 658 is transferred. Π represents the transfer from all other scales to the scales space region
 659 of scale r and below. In the spherically averaged distributions in figure 10, the energy
 660 transfer within spherical shells of a given radius, r , was considered. The scale space
 661 representation here allows us to go further and assess both the magnitude and direction
 662 of the local scale-to-scale transfers, and the redistribution of energy at the same scale.

663 The scale space distribution of non-linear inter-scale energy transfer, Π , is shown in
 664 figure 13. It is immediately observed that the transfer is negative at all scales. However, it
 665 should be noted that this energy transfer consists of both transfer to different scales, and
 666 redistribution within the same scale. At very small scales ($r < 6\eta$) the magnitude of the
 667 non-linear inter-scale transfer is small, as viscous forces dominate in this region. At larger

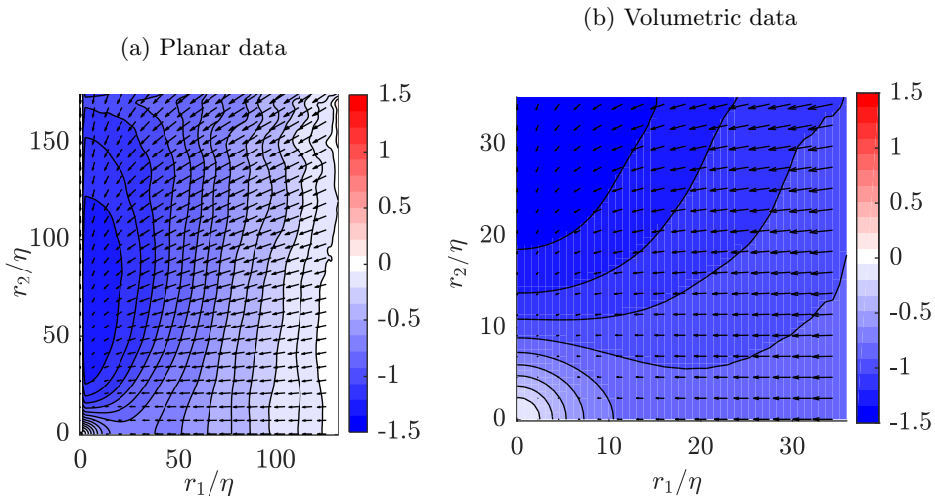


Figure 13: Distribution of Π , the non-linear inter-scale transfer rate normalized by the mean dissipation rate $\langle \epsilon \rangle$ with quiver arrows representing the direction of the flux $\langle \delta \mathbf{u} \delta q^2 \rangle$, from (a) Stereo PIV measurements, and (b) Scanning PIV measurements. Only every sixth and fourth vector shown for visibility for the Stereo and Scanning PIV results respectively.

668 scales the magnitude increases, giving rise to a strongly anisotropic distribution. For
 669 intermediate scales the magnitude is largest when r_1 is small, and the strongest variation
 670 in magnitude is observed in the r_1 -direction. The high level of anisotropy in the inter-
 671 scale transfer, where certain orientations are responsible for a greater proportion of energy
 672 transfer, may imply that the scale space orientation of energy containing structures define
 673 the amount of energy these transfer. The high magnitudes over a range of r_2 values where
 674 r_1 is small suggests high energy transfer where low velocity differences are also observed
 675 in the r_2 or axial flow direction (shown in figure 4) dominate the non-linear inter-scale
 676 energy transfer.

677 The non-linear inter-scale transport term, Π , acts not only to transfer energy between
 678 scales, but also to redistribute it within the same scale. Therefore, it is also useful to split
 679 the term into its radial and tangential contributions, Π_r and Π_t , where $\Pi = \Pi_r + \Pi_t$. The
 680 two terms are calculated in spherical coordinates using equation 3.3 and 3.4 respectively.
 681 We will first focus on the radial contributions Π_r , which is shown in figure 14.

$$\Pi_r = \frac{1}{4} \left(\frac{\partial}{\partial r} + \frac{2}{r} \right) \langle \delta u_r \delta q^2 \rangle \quad (3.3)$$

$$\Pi_t = \frac{1}{r \sin \theta} \left(\frac{\partial}{\partial \theta} \left(\langle \delta u_\theta \delta q^2 \rangle \sin \theta \right) + \frac{\partial}{\partial \phi} \langle \delta u_\phi \delta q^2 \rangle \right) \quad (3.4)$$

682 The distribution of this radial component is again highly anisotropic, and distinctly
 683 different to the total term presented previously in figure 13. The largest values of Π_r
 684 are found along the r_1 -axis, for relatively small values of r_1 , with a maximum value of
 685 $\Pi_r = -1.08 \langle \epsilon \rangle$. The radial non-linear inter-scale energy transfer is greatest where there
 686 are large velocity differences in the r_1 or radial flow direction, which again may have
 687 implications for the scale space orientation of the energy containing structures.

688 The energy cascade concept describes the inter-scale transfer of energy in the flow,

(a) Planar data

(b) Volumetric data

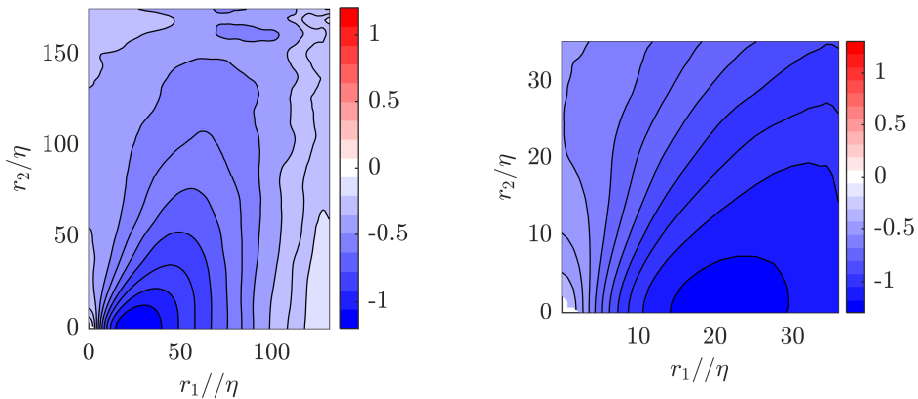


Figure 14: Radial contributions to the non-linear inter-scale transfer normalized by $\langle \epsilon \rangle$ from the Stereo and Scanning PIV data.

689 and it is of interest to evaluate the local direction of the cascade. Given that energy
 690 is injected at the large scale by the impellers and eventually converted to heat at the
 691 small scales by viscous dissipation, the overall transfer has to necessarily proceed from
 692 large to small scales in what is referred to as the forward cascade. There is however, the
 693 possibility that inverse cascade behaviour, where energy is transferred from smaller to
 694 larger scales, co-exists locally for certain orientations in scale-space. Such regions have
 695 been observed by a number of previous studies (Campagne *et al.* 2014; Gomes-Fernandes
 696 *et al.* 2015; Portela *et al.* 2017; Carter & Coletti 2018) in a wide range of flows, and
 697 specifically for von Kármán flow (Herbert *et al.* 2012) and for purely axisymmetric flows
 698 (Qu *et al.* 2017).

699 Recent studies (Gomes-Fernandes *et al.* 2015; Portela *et al.* 2017) have noted that for
 700 energy to be truly transferred in either the forward or inverse directions, two conditions
 701 must be fulfilled: first, the energy flux across scales, $\langle \overline{\delta u_r \delta q^2} \rangle$, must be either negative or
 702 positive; and second, the divergence of the flux across scales, Π_r , must also be negative
 703 or positive correspondingly. A physical interpretation of this definition, for example for
 704 forward cascade behaviour, is that energy is being transferred from larger to smaller
 705 scales as the radial component of the energy flux is negative, but also that energy
 706 accumulates at consecutively smaller scales due to the negative divergence of this flux.
 707 In other words, the amount of energy which is transferred to a given scale through
 708 the non-linear transfer is greater than the amount which is transferred away from that
 709 scale by the same mechanism. This energy is then either dissipated or removed by other
 710 mechanisms such that energy does not accumulate at any scale. Conversely for inverse
 711 cascade behaviour, energy is transferred from smaller to larger scales through Π_r , but
 712 again more energy remains than what is transferred away to still larger scales.

713 Recalling that the radial part of $\langle \delta \mathbf{u} \delta q^2 \rangle$, shown in figure 8(c) and (g) is always
 714 positive, this means that energy is always being transferred from larger to smaller scales.
 715 Evaluating this in conjunction with the scale space distribution of Π_r , which is also
 716 always negative, indicates that over all scale space orientations, the non-linear transfer
 717 exhibits forward cascade behaviour and energy is always transferred to smaller scales.
 718 This behaviour is in contrast with the results of the previous studies mentioned above,
 719 in which inverse cascade behaviour is identified in correspondence with the non-linear

term. At larger separations beyond the measurement domain, we can not confidently extrapolate the energy transfer behaviour, but it is interesting to note the increasing trend of Π_r along the r_1 -axis beyond $r_1 \approx \lambda$, which may result in more diverse cascade behaviour at larger values of r_1 .

3.3.2. Contribution of linear inter-scale transfer

While the absence of inverse cascade behaviour through the non-linear term marks a departure from the majority of previous investigations, in the present flow the magnitude of the inter-scale flux of energy from the mean flow was shown to be substantial (figure 9). Therefore, it is interesting to further consider the contribution that the mean flow exerts on the inter-scale transfer.

The linear inter-scale transfer, Π_U , is the inter-scale transfer of $\langle \delta q^2 \rangle$ associated with the interaction of the turbulent fluctuations with the mean flow. The scale space distribution of the term is presented in figure 15. At each scale, r , its value represents, similarly to the non-linear transfer, transfer of energy from all other scales to the scale r and smaller. While the spherical averaged contribution from this term ($\langle \Pi_U \rangle_\circ$ in figure 10) was shown to be modest compared to the non-linear transfer for a wide range of scales, it is clear from figure 15 that locally the magnitude of this is significant and that the quantity is highly dependent on orientation. In terms of magnitude, the local values of the linear transfer is of the same order as the non-linear transfer, but due to large cancellations, the observed distribution of positive and negative regions results in only a small contribution in an spherically averaged sense. The distribution of this transfer bears the imprint of the mean flow, which is made more apparent through the vector arrow representation of the mean energy flux, $\langle \delta \mathbf{U} \delta q^2 \rangle$, with a clear reorientation of energy within scales. The region at large r_1 and small r_2 values demonstrates a strong negative contribution to the energy budget. In contrast, the region where r_1 is small and r_2 large, is strongly positive. The high positive values of linear transfer, Π_U , appear to balance the high negative values of non-linear transfer, Π , observed in this latter region, with the similar magnitude of these opposite signed regions likely to result in an overall low magnitude of transfer in this region. Describing this distribution again highlights the significant role of the mean flow on the inter-scale transfer, which, as first shown in figure 10, is increasingly significant at larger length scales for the spherically averaged inter-scale energy budget.

Given that the linear transfer is not small enough to be neglected, it is useful to consider the total inter-scale transfer as the combination of linear and non-linear parts, $(\Pi + \Pi_U)$, which are presented in figure 16(a) and (d), with quiver arrows showing the direction of the total flux, $(\langle \delta \mathbf{u} \delta q^2 \rangle + \langle \delta \mathbf{U} \delta q^2 \rangle)$. These combined contributions are approximately isotropic at small values of r , before becoming highly dependent on orientation from $r \approx 10\eta$. A region of high negative values for the combined inter-scale transfer is observed along the radial axis for r_1 values from $\sim 10\eta - 80\eta$. As the combined inter-scale flux, $(\langle \delta \mathbf{u} \delta q^2 \rangle + \langle \delta \mathbf{U} \delta q^2 \rangle)$, is pointing towards the origin in this region, there is a net transport of energy down the scales. This combined with the strong negative values of $(\Pi + \Pi_U)$ indicates that the transport is decelerated, and thus that the inter-scale transfer contributes to an accumulation of energy in this region in scale space. As the flow is stationary, this energy will have to be removed by another mechanism. The values of $(\Pi + \Pi_U)$ in this region are around the value of the mean dissipation rate, $\langle \epsilon \rangle$. The small contributions from the remaining terms in this region indicates that total inter-scale transfer and the dissipation rate approximately balance each other in this region. However, this implies that in other regions in scale space, the other terms in the KHMH

768 equation play a more significant role in balancing the energy budget, which is discussed
769 further in §3.3.3.

770 While $(\Pi + \Pi_U)$ is negative for the majority of scales measured here, for large values
771 of r_2 the combined inter-scale transfer takes positive values. This therefore requires us to
772 re-evaluate the behaviour of the energy cascade. The cascade based on only the non-linear
773 transfer was observed to be in the forward direction, with energy transferred from larger
774 to smaller scales at all orientations and separations within the FoV. If we now define the
775 energy cascade to include the inter-scale transfer of $\langle \delta q^2 \rangle$, both due to interactions with
776 turbulent fluctuations and the mean flow, we can study its behaviour by investigating
777 the radial part of $(\Pi + \Pi_U)$, which is plotted in figure 16(b) and (e).

778 The behaviour of the inter-scale energy cascade based on this combined inter-scale
779 transfer, is significantly different from the transfer based only on the turbulent fluctua-
780 tions. The values of the combined term range from high positive values for small values
781 of θ (where the orientation of θ is defined in figure 1), transition through zero at $\theta \approx 50^\circ$,
782 and then become increasingly negative at higher angles. The contour of $(\Pi + \Pi_U) = 0$
783 is marked on the figure with a dashed green line. It is interesting to note that the
784 transition from negative to positive values of the total energy transfer coincide almost
785 exactly with the sign of the radial part of the total inter-scale flux, $(\langle \delta u_r \delta q^2 \rangle + \langle \delta U_r \delta q^2 \rangle)$,
786 which is marked with a dashed pink line in figure 16(b) and (e)). Therefore the scale
787 space distribution of energy transfer is divided into two distinct regions fulfilling the
788 requirements of opposite cascade behaviour. Energy is transferred in the forward cascade
789 direction when $50^\circ < \theta < 90^\circ$, and in the inverse direction when $0 < \theta < 50^\circ$.

790 It can also be observed that the magnitude of the radial component of $(\Pi + \Pi_U)$ is
791 significantly larger than the magnitude of the total term. To balance this, there is also
792 expected to be a significant redistribution of energy to different orientations within each
793 scale. To investigate this, the tangential part of the combined transfer, $(\Pi_t + \Pi_{U,t})$, where
794 Π_t is defined in equation 3.4, and $\Pi_{U,r}$ and $\Pi_{U,t}$ are defined in analogy to Π_r (equation
795 3.3) and Π_t . The role of $(\Pi_t + \Pi_{U,t})$ can be understood as an exchange of $\langle \delta \bar{q}^2 \rangle$ between
796 different points in scale space that sits on the same sphere with radius r (i.e. tangential
797 exchange of $\langle \delta q^2 \rangle$), and describes energy transfer within the same scale only. Note that
798 $(\Pi_t + \Pi_{U,t})$ vanishes when integrated over an infinitesimally thin spherical shell with
799 inner radius of r , and thus positive values of $(\Pi_t + \Pi_{U,t})$ at an arbitrary point \mathbf{r}_0 on the
800 shell comes at the expense of a negative contribution of equal absolute value distributed
801 over the rest of the same shell, where $\mathbf{r} \neq \mathbf{r}_0$, $|\mathbf{r}| = |\mathbf{r}_0|$. Given the interpretation of $\delta q^2(\mathbf{r})$
802 discussed in §2.4, this can be understood as a transfer of energy from all structures whose
803 characteristic size is $|\mathbf{r}_0|$ or smaller, to structures aligned with \mathbf{r}_0 of scale $|\mathbf{r}_0|$ or smaller.

804 $(\Pi_t + \Pi_{U,t})$ is presented in figures 16(c) and (f), and we see from the results that the
805 term is increasingly negative for smaller values of θ , and positive for high values of θ ,
806 almost mirroring the scale space distribution of the radial component but with a change
807 in sign. The zero crossing of the term is marked in green, which occurs when $\theta \approx 55^\circ$. This
808 therefore also demarcates the scale space distribution into two distinct regions, where the
809 forward cascade region ($50^\circ < \theta < 90^\circ$) is also accompanied by a strong redistribution
810 of energy within the same scales, from the r_1 -axis to the r_2 -axis, and vice-versa for the
811 inverse cascade region. In other words, this may imply that structures orientated along
812 the radial axis of the flow supply energy to structures oriented in the axial direction,
813 which again may be linked to the axial straining associated with the mean flow.

814 After discussing the local behaviour of the total inter-scale energy transfer, and
815 observing a significant region which experiences inverse cascade behaviour, it is finally
816 useful to examine the spherical average of this combined transfer. Figure 17 shows the

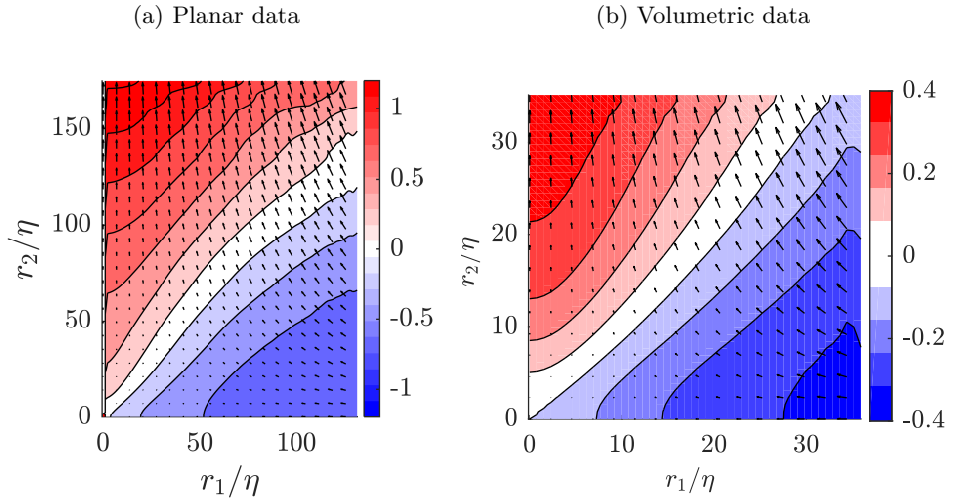


Figure 15: Distribution of Π_U , the linear inter-scale transfer of $\langle \overline{\delta q^2} \rangle$ normalised by the mean dissipation rate $\langle \epsilon \rangle$ with quiver arrows representing the direction of the flux $\langle \delta \mathbf{U} \delta q^2 \rangle$, from (a) Stereo PIV measurements, and (b) Scanning PIV measurements.

817 spherical average of the radial component of the total inter-scale transfer, $\langle (\Pi_r + \Pi_{U,r}) \rangle_\circ$.
 818 Despite regions of locally inverse cascade behaviour, the net transfer at each scale is
 819 still negative, implying a net forward cascade where energy on average is transferred
 820 from larger to smaller scales. Furthermore, it is remarkable that despite the significant
 821 magnitude of energy transfer locally, the residual of these which define the spherically
 822 averaged global cascade in the forward direction operates at a fraction of the level of
 823 the local energy transfers. It should, however, be noted that Herbert *et al.* (2012) found
 824 evidence of an overall inverse cascade in a von Kármán flow for scales larger than forcing
 825 scales. In the current study we do not have access to these scales, but the trend given in
 826 figure 17 is that the value of $\langle (\Pi_r + \Pi_{U,r}) \rangle_\circ$ is increasing for increasing separation distance,
 827 and an inverse cascade for separations larger than captured in these measurements is not
 828 unimaginable. This would to some extent also be comparable to the results of Qu *et al.*
 829 (2017), who found that in purely axisymmetric turbulence, energy is transported to larger
 830 scale in an inverse cascade. The von Kármán flow is, however, only axisymmetric in a mean
 831 sense, and is not expected obtain the exact behaviour of a purely axisymmetric flow.

832 3.3.3. Balancing the inter-scale energy budget and contributions to isotropy

833 Having described the role of the inter-scale transfer in defining the cascade behaviour,
 834 we are now left with the outstanding question of which terms contribute to balancing the
 835 energy budget in regions of the flow where the inter-scale transfer terms do not balance
 836 the dissipation rate. From figure 10 it is clear that the viscous diffusion term is important
 837 for balancing the dissipation rate at small separations. The only other term which has
 838 a positive contribution to the energy budget, in addition to Π , Π_U and D_r , is the
 839 production term associated with the mean flow gradients, \mathcal{P} . The term is plotted from the
 840 two data sets in figure 18. In general, the production increases with increasing separation
 841 distance, which was also indicated previously through the spherical average shown in
 842 figure 10. However, examining the scale space distribution of this demonstrates that it is
 843 not isotropic, and has an orientation dependence, which is especially pronounced at small
 844 separation distances. It is the scale space part (with derivatives with respect to r) which

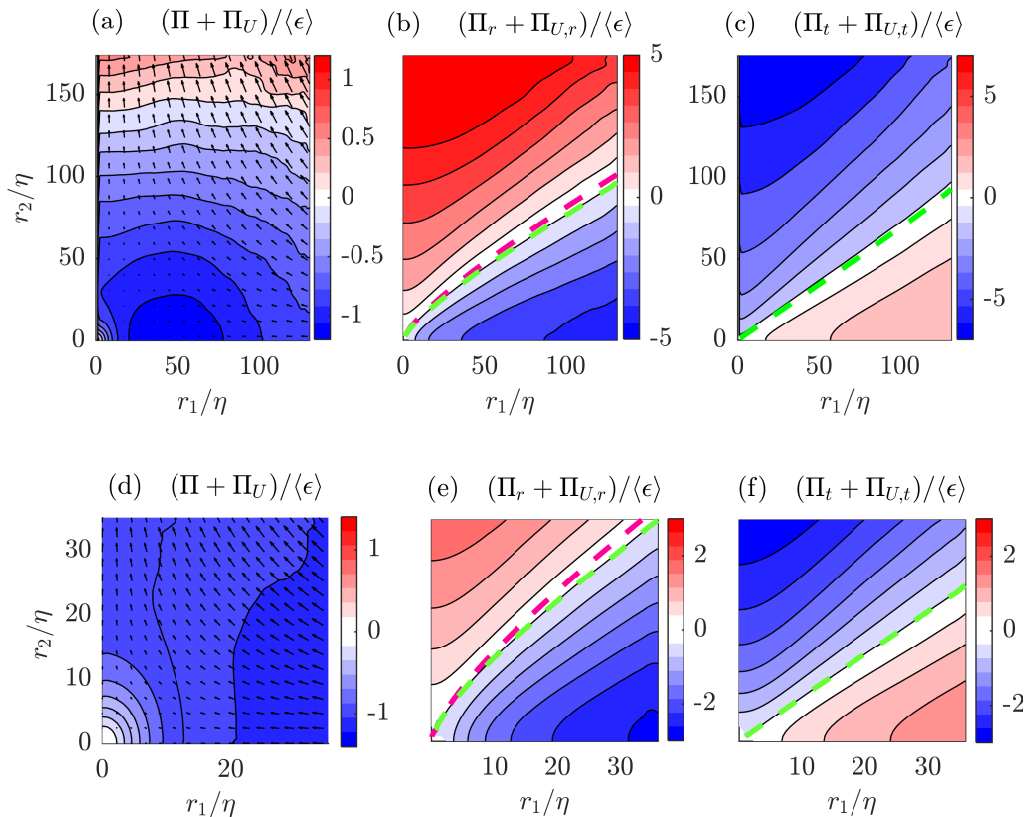


Figure 16: (a,d) Distribution of the normalised combined inter-scale transfer, $(\Pi + \Pi_U)$, with quiver arrows indicating the direction and magnitude of the combined inter-scale flux, $(\langle \delta \mathbf{u} \delta q^2 \rangle + \langle \delta \mathbf{U} \delta q^2 \rangle)$. (b,e) the radial part of the combined transfer, where $---$ indicates where $(\Pi_r + \Pi_{U,r})$ is zero, and $---$ indicates where $(\langle \delta u_r \delta q^2 \rangle + \langle \delta U_r \delta q^2 \rangle)$ is zero. (c,f) the azimuthal part of the combined transfer ($---$ indicates zero line). Based on (a,b,c) planar data and (d,e,f) volumetric data.

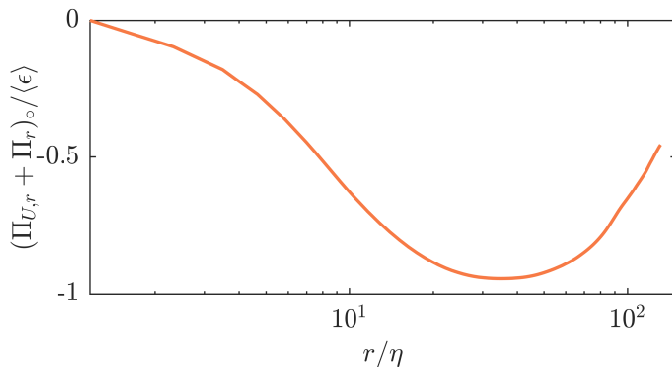


Figure 17: Spherical average of the radial part of the combined inter-scale transfer, $(\Pi_r + \Pi_{U,r})$.

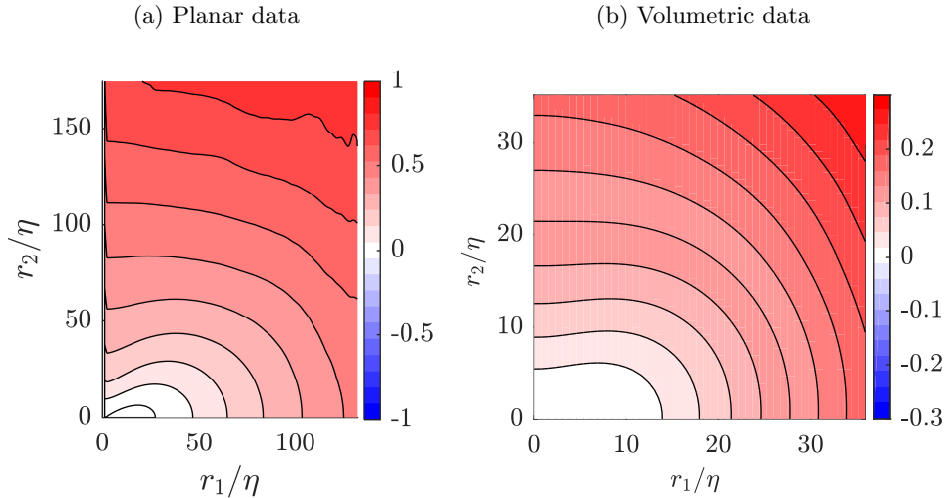


Figure 18: Distribution of the production term \mathcal{P} normalized by the mean dissipation rate $\langle \epsilon \rangle$ from (a) Stereo PIV measurements, (b) Scanning PIV measurements.

845 strongly dominates the term. The shape of the contour lines for small r indicates that
 846 there is less production along the r_1 -direction. This region of low production corresponds
 847 to the region where the dissipation rate, $\langle \epsilon \rangle$, is of same magnitude as the inter-scale
 848 transfer terms, $(\Pi + \Pi_U)$. This region in scale space is also where high values of $\langle \overline{\delta q^2} \rangle$ were
 849 previously observed, and thus higher velocity increments. Conversely, the region in the
 850 scale space map with the highest production occurs for large values of r_2 , which is where
 851 we observe lower values of $\langle \overline{\delta q^2} \rangle$. The production term therefore appears to contribute
 852 towards predominantly increasing the scale space distribution of kinetic energy most in
 853 regions where it is lowest, which could therefore be described as making the scale space
 854 distribution of energy more isotropic.

855 To test this statement, we have investigated what happens to the isotropy of $\langle \overline{\delta q^2} \rangle$ if we
 856 restrict its dynamics to contributions from particular terms of the KMH equation acting
 857 individually. For instance, to evaluate the effect of the non-linear inter-scale transfer is
 858 reduced equation 2.10 to $A_t = \Pi$. We evaluated finite differences between isotropy of the
 859 measured $\langle \overline{\delta q^2} \rangle$ and of $\langle \overline{\delta q^2} \rangle$ after a short period Δt of its assumed simplified evolution.
 860 This can be expressed as:

$$\Delta \sigma_{\langle \overline{\delta q^2} \rangle} = \sigma_{\langle \overline{\delta q^2} + A_t \Delta t \rangle} - \sigma_{\langle \overline{\delta q^2} \rangle} \quad (3.5)$$

861 Results are displayed in figure 19. As expected from the qualitative argument above
 862 the production contributes to a more isotropic distribution, particularly for small and
 863 intermediate scales. While the turbulent transport term, T_u , does not change the isotropy
 864 of the flow significantly, both linear and non-linear inter-scale transport terms have
 865 a significant effect. Π contributes to making the distribution of $\langle \overline{\delta q^2} \rangle$ more isotropic,
 866 whereas Π_U balances all of the other terms by contributing to a more anisotropic
 867 distribution of energy.

868

3.4. Flow homogeneity

869

870

871

The central region of the von Kármán mixing flow has earlier been referred to as homogeneous (Worth 2010; Lawson 2015; Kuzzay *et al.* 2015; Debue *et al.* 2018a). This assumption was further supported by the characterisation of the flow in Appendix B,

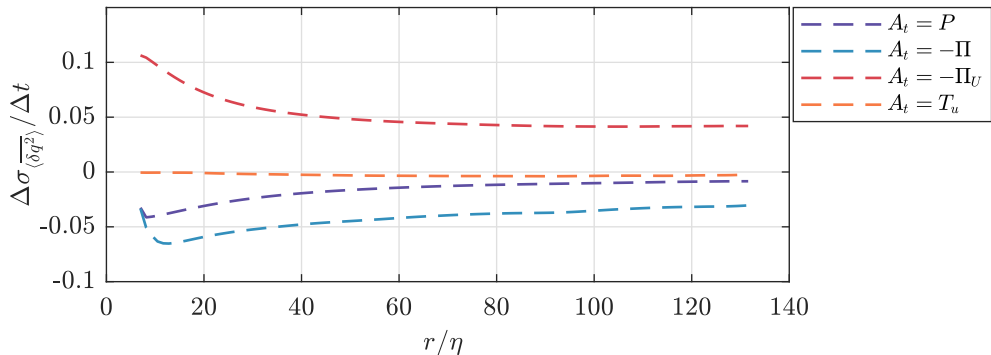


Figure 19: Influence of different terms in the KMH equation on isotropy of the distribution of $\langle \delta q^2 \rangle$.

872 where the spatial variations of the local RMS-value of the turbulent fluctuations did
 873 not vary with more than 1.9% for the Stereo PIV data, and 0.7% for the Scanning PIV
 874 data. The effect of homogeneous turbulent fluctuations would be expected to result in
 875 the mean transport of $\langle \delta q^2 \rangle$ by turbulent fluctuations, T_u , to be zero. However, figure
 876 10 previously showed that the spatial average of T_u is not zero, but reaches a value
 877 of $-0.1\langle \epsilon \rangle$ at $r = 25\eta$, and keeps decreasing to a maximum of $-0.22\langle \epsilon \rangle$ at the largest
 878 separation distance. It is therefore of interest to investigate the local distribution of T_u ,
 879 which is presented for the two data sets in figure 20. The term is zero for small values of
 880 r , before becoming negative for larger values. The distribution of T_u is close to isotropic
 881 at small scales, before becoming dependent on orientation for $r > 40\eta$. The dependence
 882 of this term on scale space orientation warrant a more thorough investigation of the flow
 883 homogeneity, and in particular the skewness factor, which is defined as:

$$S_{u_i} = \frac{\overline{u_i^3}}{u_i^2 3/2} \quad (3.6)$$

884 The mean skewness factor for different velocity components is shown in table 3,
 885 with small negative values for each component. However, plotting the distribution of
 886 skewness over the domain in figure 21 shows the local values of the skewness of u_1 varies
 887 significantly in magnitude from -0.12 to 0.12. The skewness varies almost linearly with
 888 radial location, transitioning from negative to positive values from left to right hand sides
 889 of the measurement domain. This variation indicates that the turbulent fluctuations are
 890 not in fact completely homogeneous, even in the center region of the tank, and that
 891 the probability for high values of the fluctuations occurring in the direction opposite
 892 to the mean flow is higher than the probability of high fluctuations in the direction of
 893 the mean flow. In other words, there tends to be large sweeps outwards, away from the
 894 symmetry axis more often than sweeps inwards, towards the symmetry axis. The lack of
 895 homogeneity in this higher order metric is consistent with the non-zero transport of $\langle \delta q^2 \rangle$
 896 by the turbulent fluctuations, T_u , which also depends on the velocity triple-products.

897 4. Conclusions

898 Fully resolved planar Stereoscopic PIV and volumetric Scanning PIV experiments were
 899 conducted to study the inter-scale energy budget in a von Kármán mixing flow. A large

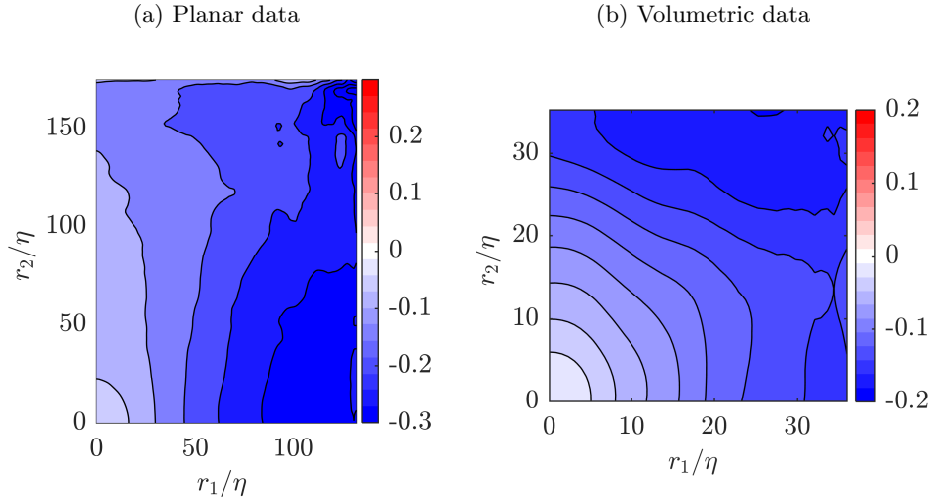


Figure 20: Distribution of the turbulent diffusion of $\langle \overline{\delta q^2} \rangle$, T_u , normalized by the mean dissipation rate $\langle \epsilon \rangle$ from (a) Stereo PIV measurements, (b) Scanning PIV measurements.

	Stereo PIV	Scanning PIV
$\langle S_{u_1} \rangle$	-0.02	-0.01
$\langle S_{u_2} \rangle$	-0.02	-0.01
$\langle S_{u_3} \rangle$	-0.01	0.03

Table 3: Skewness factor of different velocity components from the two data sets.

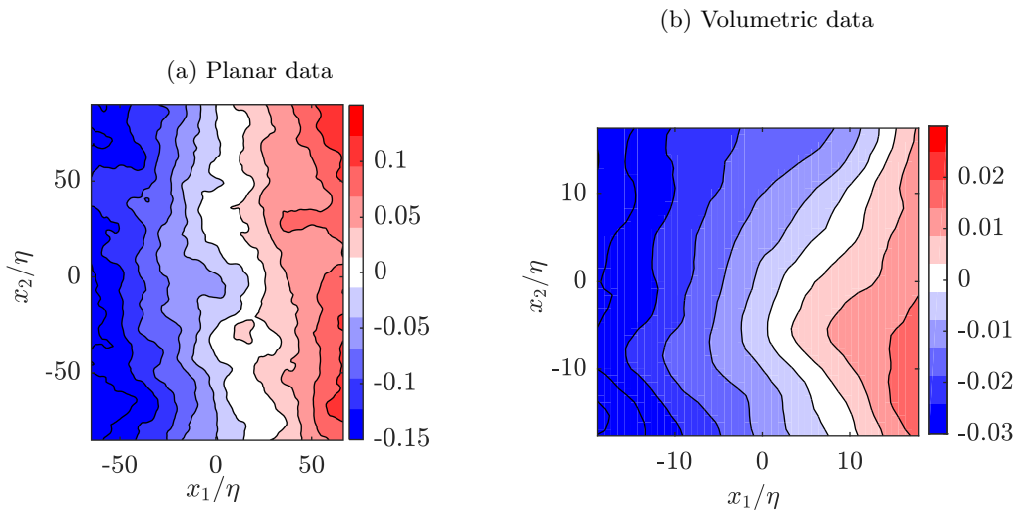


Figure 21: Spatial distribution of the skewness factor of u_1 , S_{u_1} , from (a) Stereo PIV measurements, (b) Scanning PIV measurements.

900 number measurements were made at the center of the tank, where the mean flow is
901 much weaker than the turbulent fluctuations. An initial characterisation of the flow
902 was performed together with a comparison of the two data sets. Mean and turbulent
903 flow quantities closely resembled previous measurements made in von Kármán mixing
904 flows, and the fidelity of measurements was quantified. Furthermore, good agreement
905 was observed between the two data sets, with the very similar flow statistics providing
906 in particular confidence in the quality of the volumetric measurements.

907 Both the distribution and transfer of kinetic energy in the flow were observed to
908 be anisotropic at all scales. The longitudinal second order structure function was also
909 investigated, and showed a strong directional dependency, which, when normalized ac-
910 cording to Kolmogorov's 2/3rd-law, led to a directional dependency of the Kolmogorov
911 constant C_2 , which is consistent with the predictions given in (Lumley 1967; Biferale
912 & Procaccia 2005) for turbulent shear flows. The transfer due to turbulent fluctuations
913 and the mean flow were quantified, and it was found that the latter dominated the local
914 energy transfer in contrast to previous work. Therefore, despite the small magnitude of
915 the mean flow the large gradients in all directions result in significant contributions to
916 the energy flux at large separation distances. This flow configuration is the first to give
917 rise to such significant mean flow interactions with the inter-scale transfer of turbulent
918 kinetic energy, which enables a novel assessment of the energy cascade behaviour. Further
919 investigation demonstrated that the transfer due to the turbulent fluctuations was always
920 in the downscale direction, with energy transferred unidirectionally from larger to smaller
921 scales, and certain scale space regions were shown to dominate this transfer. In contrast
922 the inter-scale transfer due to the mean flow contained regions of both upscale and
923 downscale transfer.

924 Following this the Kármán Howarth Monin Hill equation was used as a tool to
925 investigate the inter-scale energy budget. In a spherically averaged sense at small to
926 moderate flow scales ($6\eta < r < 90\eta$) the non-linear energy transfer term dominates
927 the energy budget, providing some support to the assumption of simple inertial sub-
928 range cascade behaviour, where dissipation and energy transfer are balanced. While the
929 spherically averaged value of the non-linear inter-scale transfer, $\langle \Pi \rangle_\circ$, is neither constant,
930 nor equal to the dissipation rate $\langle \epsilon \rangle$ across the scales investigated in this study, the
931 assumption is still a reasonably accurate assessment of the broad flow behaviour. At
932 larger scales the effects of the mean flow become more significant through the interaction
933 of turbulent production and mean flow gradients, restricting the further applicability of
934 this simple picture.

935 Further examination of the non-linear inter-scale transfer term in scale space showed
936 that the radial energy flux from scale to scale is always negative, indicating a cascade
937 of energy in the forward direction; where energy at all scale space orientations is passed
938 from larger to smaller scale. The radial part of the inter-scale transfer term, Π_r , is also
939 always negative, which also points towards forward cascade behaviour. However, when
940 including the linear transfer caused by the mean flow, two distinct regions of the flow are
941 observed, where we have forward cascade behaviour in one region and inverse cascade
942 in the other. Despite occupying a similar sized region of scale space, in an spherically
943 averaged sense the combined energy transfer is still downscale. However, the emergence
944 of such a large region of inverse cascade behaviour connected directly to the mean flow
945 presents the opportunity to understand more about the transfer of energy from scale
946 to scale. Additionally, the trend of the total inter-scale transfer is such that a change
947 of direction of the energy cascade might be possible at larger scales, which would be in
948 agreement with the findings of Herbert *et al.* (2012). Despite its significant contributions
949 to inter-scale transfer, the mean flow was shown to have small contributions to the transfer

of $\langle \delta q^2 \rangle$ in physical space, which coincides with the results of Marié & Daviaud (2004) for transport of angular momentum in the center region of a von Kármán flow.

Finally, scale space evaluation of other significant terms in the KMH equation were used to show that energy contributions from the turbulent production term balances the energy budget in regions exhibiting inverse cascade behaviour. Analysis was also conducted to assess the influence of various terms on the scale space distribution of $\langle \delta q^2 \rangle$, and it was observed that the production term, \mathcal{P} , and the non-linear term Π both act towards increasing the isotropy of the scale space distribution of $\langle \delta q^2 \rangle$, whereas the linear term, Π_U acts to make this more anisotropic. Finally, a non-negligible contribution from the turbulent diffusion term, T_u , was also observed, and coupled to a spatial variation of the skewness of the fluctuating velocity components.

It is striking that despite a high level of local activity in scale space for a range of sources, the balance of these in a spherically averaged sense results in only modest contributions to the total energy budget, meaning non-linear inter-scale energy transfer approximately balances dissipation for moderate flow scales. Therefore, this simplistic picture of energy transfer does not capture the strikingly varied picture arising from a more complete overview of energy transfer in this well known turbulent flow.

Acknowledgements

The authors gratefully acknowledge the support of the Max Planck Society and EuHIT: European High Performance Infrastructures in Turbulence, funded under the European Unions Seventh Framework Programme (FP7/2007-2013) Grant Agreement No. 312778.

Declaration of Interests

The authors report no conflict of interest.

Appendix A. Measurement error analysis and determination of confidence intervals

A.1. Measurement error analysis

Following the flow characterisation, the accuracy of the two data sets is quantified through an assessment of the measurement errors. We follow initially the methodology of Romano *et al.* (1999) and Benedict & Gould (1998), who estimated the variance of the random measurement error, ε_i , through the correlation of velocity fluctuations, $\langle R_{ii}(\mathbf{x}, \mathbf{r}) \rangle = \overline{u_i(\mathbf{x}, t) u_i(\mathbf{x} + \mathbf{r}, t)}$, where the measured component velocities at location, \mathbf{x} , are a combination of the true velocity and the measurement error, so that $u_i(\mathbf{x}, t) = u_{i,true}(\mathbf{x}, t) + \varepsilon_i$. While the complete shape of this correlation function is not known, its shape when the separation distance, $|\mathbf{r}|$, tends to zero is known to be parabolic (Pope 2005). Assuming that the error is a normally distributed random value, and is neither spatially correlated nor correlated with the measured velocity field, the contribution of this error to $\langle R_{ii}(\mathbf{x}, \mathbf{r}) \rangle$ will only appear at $|\mathbf{r}| = 0$. The RMS value of ε_i can thus be found by fitting a parabolic surface into $\langle R_{ii} \rangle$ for small separation distances where $|\mathbf{r}|$ is close to zero, and then comparing the measured and fitted values of $\langle R_{ii} \rangle$ at $|\mathbf{r}| = 0$. Applying this method, the errors for the Stereo and Scanning PIV data were calculated, using only every second vector for the Stereo PIV data and every fourth vector from the Scanning PIV data, to remove correlation from vectors calculated on overlapping interrogation windows/volumes. The fit was based on the 2nd to 5th point only, with

	$\langle \varepsilon_{1,rms} \rangle / \langle u_{rms} \rangle$	$\langle \varepsilon_{2,rms} \rangle / \langle u_{rms} \rangle$	$\langle \varepsilon_{3,rms} \rangle / \langle u_{rms} \rangle$
Stereo PIV	0.30%	0.25%	0.38%
Scanning PIV	0.09%	0.33%	0.22%

Table 4: Estimates of rms values of random error ε_i expressed as a percentage of the mean fluctuation magnitude, $\langle u_{rms} \rangle$.

993 values reported in table 4. It is observed that the random errors are of an insignificant
 994 order of magnitude ($<0.3\%$) compared to the mean fluctuations, demonstrating a high
 995 signal to noise ratio (SNR).

996 A second method of evaluating the measurement uncertainty is through the divergence
 997 free criteria. As the flow is assumed to be incompressible, the sum of diagonal velocity
 998 gradient tensor terms should be zero. The correlation coefficient calculated from the
 999 joint PDF of gradient components from the Scanning PIV data takes a value of 0.867,
 1000 compared to an ideal value of unity. This high correlation value demonstrates that large
 1001 departures from continuity are rare, and compares very well to other previous studies
 1002 (Casey *et al.* 2013; Worth 2010; Ganapathisubramani *et al.* 2007), demonstrating the high
 1003 fidelity of the measurements. To translate this into an estimate of the uncertainty in the
 1004 gradients, the standard deviation of the sum $\partial u_i / \partial x_i$ (which from continuity should be
 1005 zero), i.e. $\sqrt{3}\sigma_{grad}$, was calculated for the Scanning PIV data using equation A 1.

$$\sqrt{3}\sigma_{grad} = \sqrt{\frac{1}{N_s} \left(\frac{\partial u_i}{\partial x_i} \right)^2} \quad (\text{A } 1)$$

1006 The results in a standard deviation for each particular derivative (assuming they are
 1007 independent of each other) of $\sigma_{grad}\tau = 0.12$, where $\tau = \sqrt{\nu/\langle \epsilon \rangle}$ is the Kolmogorov time
 1008 scale, again demonstrating only very small deviations from the divergence free condition.

1009 A.2. Determination of confidence intervals

1010 Where possible an effort has been made to put confidence intervals on certain quanti-
 1011 ties. The underlying distribution of the variables in questions is not known, and therefore
 1012 to estimate these the bootstrap method (Efron & Tibshirani 1994) may in theory be
 1013 used. However, due to the extremely large data sets, excessive computational time makes
 1014 it unrealistic to use the standard bootstrap approach in this case, and therefore an
 1015 alternative method was applied to give an indicative estimate of the uncertainty. The
 1016 standard bootstrap approach was applied to a small subset of our dataset (of size
 1017 n), yielding approximations of variances of different statistics evaluated based on the
 1018 restricted dataset, $\tilde{\sigma}^2$. In the second step, the variances was scaled to the size of the full
 1019 dataset, N_s , as expressed by equation A 2, using asymptomatic properties of bootstrap
 1020 predictions (Bickel & Freedman 1981). In this work, we have used $n = 100$, and repeated
 1021 the calculations for 1000 subsets.

$$\sigma = \frac{\tilde{\sigma}}{\sqrt{N_s/n}} \quad (\text{A } 2)$$

1022 This value is then used to define 95% confidence intervals. The procedure was evaluated
 1023 with different values of n to confirm that the scaling of $\tilde{\sigma}$ did in fact vary with $1/\sqrt{N_s/n}$
 1024 as expected.

	Stereo PIV			Scanning PIV		
	$i = 1$	$i = 2$	$i = 3$	$i = 1$	$i = 2$	$i = 3$
$j = 1$	2.32	-0.01	0.02	2.28	0.01	0.02
$j = 2$	-0.01	0.95	-0.02	0.01	0.98	0.01
$j = 3$	0.02	-0.02	2.24	0.02	0.01	2.34

Table 5: Reynolds stresses normalized by impeller frequency and radius, $\langle \overline{u_i u_j} \rangle / (\frac{D}{2} f)^2$

Appendix B. Flow characterisation

B.1. Flow characterisation and comparison of data sets

B.1.1. Velocity fluctuation statistics

The RMS of the spatial mean fluctuations in the various flow directions have a maximum deviation from the spatio-temporal mean value, $\sqrt{\langle \overline{u_i^2} - \langle \overline{u_i^2} \rangle} / \sqrt{\langle \overline{u_i^2} \rangle}$, of 1.3%, 1.9% and 1.3% in x_1 -, x_2 - and x_3 -direction respectively from the Stereo PIV data, and 0.4%, 0.7%, and 0.3% from the Scanning PIV data, implying that the flow is homogeneous relative to the mean flow. The velocity gradients also appear to be approximately locally homogeneous, with the largest spatial variation of the square of the gradients varying from $\langle (\langle (\partial u_1 / \partial x_2)^2 \rangle - \langle (\partial u_1 / \partial x_2)^2 \rangle) / \langle (\partial u_1 / \partial x_2)^2 \rangle \rangle = 7.4\%$ to $\langle (\langle (\partial u_2 / \partial x_1)^2 \rangle - \langle (\partial u_2 / \partial x_1)^2 \rangle) / \langle (\partial u_2 / \partial x_1)^2 \rangle \rangle = 13.6\%$ from the Stereo PIV data, and from $\langle (\langle (\partial u_3 / \partial x_1)^2 \rangle - \langle (\partial u_3 / \partial x_1)^2 \rangle) / \langle (\partial u_3 / \partial x_1)^2 \rangle \rangle = 3.4\%$ to $\langle (\langle (\partial u_3 / \partial x_3)^2 \rangle - \langle (\partial u_3 / \partial x_3)^2 \rangle) / \langle (\partial u_3 / \partial x_3)^2 \rangle \rangle = 8.4\%$ from the Scanning PIV data.

Table 5 shows an overview of the mean Reynolds stresses. In an isotropic flow, the diagonal values of the Reynolds stresses would be equal, and the remaining stresses would be zero, while in an axisymmetric flow, the tensor should follow relation:

$$\overline{u_i u_j} = A \delta_{ij} + B n_i n_j \quad (\text{B1})$$

where \mathbf{n} is the unit vector for the symmetry axis and δ_{ij} is the Kronecker delta (Batchelor & Taylor 1946).

The strong shear generated by the counter rotating flow creates high turbulent fluctuations, and neither the mean flow nor the turbulent fluctuations in the tank are isotropic. There is, however, an axisymmetry along the x_2 -axis, with the constants in equation B1 equal to $A / (\frac{D}{2} f) \approx 2.3$ and $B / (\frac{D}{2} f) \approx 1.0$. Previous studies of von Kármán mixing flow have found that the ratio between fluctuations in the radial and axial directions is ~ 1.5 , while the off-diagonal terms are expected to be close to zero (Voth *et al.* 1998). Therefore, the current measured ratios of 1.55 and 1.52 from the Stereo and Scanning PIV data agree well with previous results (Voth *et al.* 2002; Worth 2010; Lawson 2015). Furthermore, the predicted Reynolds stresses from the two data sets are very similar, and vary by a maximum of $\overline{u_i u_j} / (\frac{D}{2} f)^2 = 0.1$ for the square of the out-of-plane velocity, which corresponds to 4.3% of u_{rms} .

The mean flow gradients are approximately constant across the measurement volume, and the values collected from the two data sets are presented in table 6. The results are similar, with a maximum deviation of $\langle \frac{\partial U_i}{\partial x_i} \rangle / f = 0.25$, again for the out-of-plane component. The result of constant gradients is an expected constant dissipation rate. Based on the Scanning PIV data has small local variations: $\langle (\nu \frac{\partial u_i}{\partial x_j} \frac{\partial u_i}{\partial x_j} - \epsilon)^2 \rangle / \langle \epsilon \rangle = 0.8\%$. The dissipation rate is therefore assumed to have a constant value across the FoV.

	$\langle \frac{\partial U_1}{\partial x_1} \rangle / f$	$\langle \frac{\partial U_2}{\partial x_2} \rangle / f$	$\langle \frac{\partial U_3}{\partial x_3} \rangle / f$
Stereo PIV	-2.10	4.00	-1.95
Scanning PIV	-2.00	4.15	-2.15

Table 6: Mean gradients in the flow normalized by impeller frequency calculated from the two data sets.

B.1.2. Comparison of flow topology between measurement methods

The flow topology is briefly characterised in terms of the distribution of enstrophy and dissipation, and then invariant quantities. Given that the full velocity gradient tensor is available from the volumetric measurements, the true dissipation rate can be directly calculated without assumptions using equation B 2.

$$\epsilon_{true} = 2\nu \overline{s_{ij}s_{ij}} \quad (\text{B 2})$$

where the strain rate tensor, s_{ij} , is evaluated from equation B 3,

$$s_{ij} = \frac{1}{2} \left(\frac{\partial u_i}{\partial x_j} + \frac{\partial u_j}{\partial x_i} \right). \quad (\text{B 3})$$

However, the same calculations cannot be made using the planar data, as the velocity gradient tensor is incomplete. Therefore, the dissipation rate is calculated using assumptions of axisymmetry, with the missing terms replaced according to George & Hussein (1991) using equation B 4.

$$\begin{aligned} \epsilon_{axi} = 2\nu & \left(\overline{\left(\frac{\partial u_1}{\partial x_1} \right)^2} + \overline{\left(\frac{\partial u_2}{\partial x_2} \right)^2} + \overline{\left(\frac{\partial u_3}{\partial x_3} \right)^2} + \overline{\left(\frac{\partial u_1}{\partial x_2} \right)^2} \right. \\ & \left. + \overline{\left(\frac{\partial u_2}{\partial x_1} \right)^2} + 2 \overline{\frac{\partial u_1}{\partial x_2} \frac{\partial u_2}{\partial x_1}} + \overline{\left(\frac{\partial u_3}{\partial x_1} \right)^2} + \overline{\frac{1}{2} \frac{\partial u_1}{\partial x_1} \frac{\partial u_3}{\partial x_3}} \right) \end{aligned} \quad (\text{B 4})$$

The relation in equation B 4 is usually used to estimate the mean dissipation rate, which also is the case for this work. In addition we use the instantaneous values of the two dissipation rates, ϵ'_{true} and ϵ'_{axi} (where ' implies that it is the instantaneous values which is considered) to compare the joint PDF and PDF of the two terms shown in figure 22, which, when compared to the distribution of the full dissipation, ϵ_{true} , appears to be a good approximation. However, we will still like to emphasize that the instantaneous estimations of ϵ'_{axi} are solely used to compare the two datasets. To assess the level of local axisymmetry, a test was performed by using the following relations derived in George & Hussein (1991), where it is stated that $K_1 = K_2$ in axisymmetric flow:

$$K_1 = 2 \left\langle \overline{\left(\frac{\partial u_2}{\partial x_2} \right)^2} \right\rangle / \left\langle \overline{\left(\frac{\partial u_1}{\partial x_2} \right)^2} \right\rangle \quad (\text{B 5})$$

$$K_2 = 2 \left\langle \overline{\left(\frac{\partial u_2}{\partial x_2} \right)^2} \right\rangle / \left\langle \overline{\left(\frac{\partial u_3}{\partial x_2} \right)^2} \right\rangle \quad (\text{B 6})$$

The values from the Stereo PIV data was calculated to be 0.94 and 0.93 for K_1 and K_2 respectively, giving a good indication that the flow is behaving locally axisymmetric.

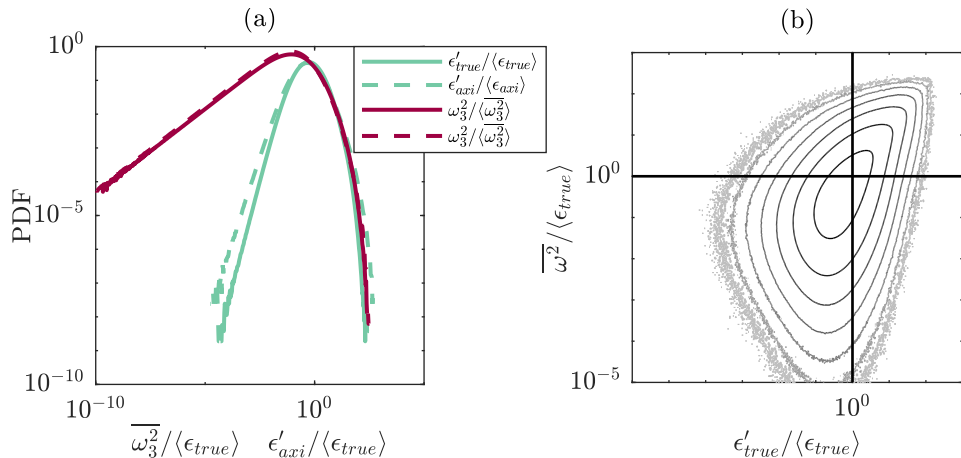


Figure 22: (a) PDFs of dissipation rate ϵ'_{true} , the dissipation rate based on axisymmetric assumptions ϵ'_{axi} , and the third component of the vorticity, ω_3^2 . Solid lines from Scanning PIV data, and dashed lines from Stereo PIV data. (b) Joint PDF of dissipation rate ϵ'_{true} and the enstrophy, ω^2 from Scanning PIV data. The contours are logarithmically spaced from 10^{-5} to 10^{-2} .

1082 To test the validity of these assumptions, and again compare the calculated velocity
 1083 gradients of the two data sets, the probability density function (PDF) of ϵ'_{axi} , ϵ'_{true} and
 1084 the third component of the vorticity vector squared, ω_3^2 (where $\boldsymbol{\omega} = \nabla \times \mathbf{u}$), based on the
 1085 two datasets are compared in figure 22(a). There is an almost exact overlap of the PDFs
 1086 of ω_3^2 based on the two datasets, indicating that the gradients based on the two datasets
 1087 have a very similar behaviour. As for the dissipation, the shape of the distributions of
 1088 ϵ'_{axi} and ϵ'_{true} is similar, but the planar data tends to slightly overestimate extreme high
 1089 and low dissipation events compared to the PDF of the full dissipation rate calculated
 1090 from the volumetric data.

1091 To evaluate the distribution of high gradient regions, the joint probability density
 1092 function (JPDF) of enstrophy, ω^2 , and dissipation rate is given in figure 22(b). The
 1093 distribution shows good agreement with previous studies (Yeung *et al.* 2012; Carter &
 1094 Coletti 2018; Worth & Nickels 2011), demonstrating characteristic associated with high
 1095 Reynolds number turbulent flows. The first quadrant, where high values of both ϵ and ω^2
 1096 are present has an almost symmetric, pointed shape, indicating that extreme high values
 1097 of the two terms occur simultaneously (Worth & Nickels 2011). The close agreement
 1098 observed between the velocity gradient statistics using the two different measurement
 1099 methods provides confidence that the more technically challenging volumetric measure-
 1100 ments are consistent with the planar measurements, and that the volumetric data set is
 1101 capable of capturing the important flow gradient characteristics.

REFERENCES

- 1102 ARAD, ITAI, L'VOV, VICTOR S. & PROCACCIA, ITAMAR 1999 Correlation functions in isotropic
 1103 and anisotropic turbulence: the role of the symmetry group. *Physical review. E, Statistical
 1104 physics, plasmas, fluids, and related interdisciplinary topics* **59** 6, 6753–65.
 1105 BATCHELOR, G.K. 1951 Note on a class of solutions of the Navier-Stokes equations representing
 1106 steady rotationally-symmetric flow. *The Quarterly Journal of Mechanics and Applied
 1107 Mathematics* **4** (1), 29–41.

- 1108 BATCHELOR, G.K. 1969 Computation of the energy spectrum in homogeneous two dimensional
1109 turbulence. *The Physics of Fluids* **12** (12).
- 1110 BATCHELOR, G.K. & TAYLOR, G.I. 1946 The theory of axisymmetric turbulence. *Proceedings*
1111 *of the Royal Society of London. Series A. Mathematical and Physical Sciences* **186**.
- 1112 BENEDICT, L.H. & GOULD, R.D. 1998 Concerning time and length scale estimates made from
1113 burst-mode LDA autocorrelation measurements. *Experiments in Fluids* **24** (3), 246–253.
- 1114 BICKEL, PETER J. & FREEDMAN, DAVID A. 1981 Some asymptotic theory for the bootstrap.
1115 *Ann. Statist.* **9** (6), 1196–1217.
- 1116 BIFERALE, L. & PROCACCIA, I. 2005 Anisotropy in turbulent flows and in turbulent transport.
1117 *Phys. Rep* pp. 43–164.
- 1118 BONN, D., COUDER, Y., VAN DAM, P.H.J. & DOUADY, S. 1993 From small scales to large scales
1119 in 3-dimensional turbulence : the effect of diluted polymers. *Physical Review E* **47** (1),
1120 R28–R31.
- 1121 BOURGOIN, M., VOLK, R., PLIHON, N., AUGIER, P., ODIER, P. & PINTON, J.F. 2006 An
1122 experimental bullard–von kármán dynamo. *New Journal of Physics* **8** (12), 329–329.
- 1123 CADOT, O., DOUADY, S. & COUDER, Y. 1995 Characterization of the low-pressure filaments
1124 in a three-dimensional turbulent shear flow. *Physics of Fluids* **630** (7).
- 1125 CAMPAGNE, A., GALLET, B., MOISY, F. & CORTET, P.P. 2014 Direct and inverse energy
1126 cascades in a forced rotating turbulence experiment. *Physics of Fluids* **26** (12), 125112.
- 1127 CARTER, DOUGLAS W. & COLETTI, FILIPPO 2018 Small-scale structure and energy transfer in
1128 homogeneous turbulence. *Journal of Fluid Mechanics* **854**, 505–543.
- 1129 CASCIOLA, C.M., GUALTIERI, P., BENZI, R. & PIVA, R. 2003 Scale-by-scale budget and
1130 similarity laws for shear turbulence. *Journal of Fluid Mechanics* **476**, 105–114.
- 1131 CASEY, T.A., SAKAKIBARA, J. & THORODDSEN, S.T. 2013 Scanning tomographic particle
1132 image velocimetry applied to a turbulent jet. *Physics of Fluids* **25** (2).
- 1133 CHANG, K., BEWLEY, G.P. & BODENSCHATZ, E. 2012 Experimental study of the influence of
1134 anisotropy on the inertial scales of turbulence. *Journal of Fluid Mechanics* **692**.
- 1135 CIMARELLI, A., DE ANGELIS, E., JIMÉNEZ, J. & CASCIOLA, C. M. 2016 Cascades and wall-
1136 normal fluxes in turbulent channel flows. *Journal of Fluid Mechanics* **796**, 417–436.
- 1137 CORTET, P. P., DIRIBARNE, P., MONCHAUX, R., CHIFFAUDEL, A., DAVIAUD, F. &
1138 DUBRULLE, B. 2009 Normalized kinetic energy as a hydrodynamical global quantity
1139 for inhomogeneous anisotropic turbulence. *Physics of Fluids* **21** (2), 025104, arXiv:
1140 <https://doi.org/10.1063/1.3073745>.
- 1141 DANAILA, L., ANSELMET, F. & ANTONIA, R.A. 2002 An overview of the effect of large-scale
1142 inhomogeneities on small-scale turbulence. *Physics of Fluids - PHYS FLUIDS* **14**, 2475–
1143 2484.
- 1144 DANAILA, L., ANSELMET, F., ZHOU, T. & ANTONIA, R.A. 1999 A generalization of yaglom’s
1145 equation which accounts for the large-scale forcing in heated decaying turbulence. *Journal*
1146 *of Fluid Mechanics* **391**, 359–372.
- 1147 DANAILA, L., ANSELMET, F., ZHOU, T. & ANTONIA, R.A. 2001 Turbulent energy scale budget
1148 equations in a fully developed channel flow. *Journal of Fluid Mechanics* **430**, 87–109.
- 1149 DAVIDSON, P. 2004 *Turbulence: An Introduction for Scientists and Engineers*. Oxford University
1150 Press.
- 1151 DEBUE, P., KUZZAY, D., SAWI, E. W., DAVIAUD, F., DUBRULLE, B., CANET, L., ROSSETTO,
1152 V. & WSCHEBOR, N. 2018a Experimental test of the crossover between the inertial and
1153 the dissipative range in a turbulent swirling flow. *Phys. Rev. Fluids* **3**.
- 1154 DEBUE, P., SHUKLA, V., KUZZAY, D., FARANDA, D., SAW, E.-W., DAVIAUD, F. & DUBRULLE,
1155 B. 2018b Dissipation, intermittency, and singularities in incompressible turbulent flows.
1156 *Phys. Rev. E* **97**, 053101.
- 1157 DEISLER, ROBERT G. 1961 Effects of inhomogeneity and of shear flow in weak turbulent fields.
1158 *The Physics of Fluids* **4** (10), 1187–1198.
- 1159 DEISLER, R. G. 1981 Spectral energy transfer for inhomogeneous turbulence. *The Physics of*
1160 *Fluids* **24** (10), 1911–1912.
- 1161 DIMOTAKIS, P.E. 2005 Turbulent mixing. *Annual Review of Fluid Mechanics* **37** (1), 329–356.
- 1162 DUBRULLE, BRENGRE 2019 Beyond Kolmogorov cascades. *Journal of Fluid Mechanics* **867**, P1.
- 1163 EFRON, B. & TIBSHIRANI, R.J. 1994 *An Introduction to the Bootstrap*. Chapman and Hall/CRC.
- 1164 GANAPATHISUBRAMANI, B., LAKSHMINARASIMHAN, K. & CLEMENS, N.T. 2007 Determination

- of complete velocity gradient tensor by using cinematographic stereoscopic PIV in a turbulent jet. *Experiments in Fluids* **42** (6).
- 1167 GEORGE, W.K. & HUSSEIN, J.H. 1991 Locally axisymmetric turbulence. *Journal of Fluid*
1168 *Mechanics* **233**, 1–23.
- 1169 GODEFERD, F.S. & CAMBON, C. 1994 Detailed investigation of energy transfers in homogeneous
1170 stratified turbulence*. *Physics of Fluids* **6** (6), 2084–2100.
- 1171 GOMES-FERNANDES, R., GANAPATHISUBRAMANI, B. & VASSILICOS, J.C. 2015 The energy
1172 cascade in near-field non-homogeneous non-isotropic turbulence. *Journal of Fluid*
1173 *Mechanics* **771**, 676–705.
- 1174 HERBERT, E., DAVIAUD, F., DUBRULLE, B., NAZARENKO, S. & NASO, A. 2012 Dual non-
1175 Kolmogorov cascades in a von Kármán flow. *EPL (Europhysics Letters)* **100** (4), 44003.
- 1176 HILL, R.J. 2002 Exact second-order structure-function relationships. *Journal of Fluid Mechanics*
1177 **468**, 317–326.
- 1178 JONG, J. DE, CAO, L., WOODWARD, S.H., SALAZAR, J.P.L.C., COLLINS, L.R. & H. MENG, H.
1179 2009 Dissipation rate estimation from piv in zero-mean isotropic turbulence. *Experiments*
1180 *in Fluids* **46** (3).
- 1181 JUCHA, J. 2014 Time-symmetry breaking in turbulent multi-particle dispersion. PhD thesis,
1182 Georg-August University School of Science.
- 1183 JUCHA, JENNIFER, XU, HAITAO, PUMIR, ALAIN & BODENSCHATZ, EBERHARD 2014 Time-
1184 reversal-symmetry breaking in turbulence. *Phys. Rev. Lett.* **113**.
- 1185 VON KARMAN, T. & HOWARTH, L. 1938 On the statistical theory of isotropic turbulence.
1186 *Proceedings of the Royal Society of London A: Mathematical, Physical and Engineering*
1187 *Sciences* **164** (917), 192–215.
- 1188 KNUTSEN, A.N., LAWSON, J.M. & WORTH, J.R. DAWSON N.A. 2017 A laser sheet self-
1189 calibration method for scanning PIV. *Experiments in Fluids* **58** (10), 145.
- 1190 KOLMOGOROV, A. 1941 The local structure of turbulence in incompressible viscous fluid for
1191 very large Reynolds' numbers. *Akademiia Nauk SSSR Doklady* **30**, 301–305.
- 1192 KOLMOGOROV, A. N. 1962 A refinement of previous hypotheses concerning the local structure
1193 of turbulence in a viscous incompressible fluid at high Reynolds number. *Journal of Fluid*
1194 *Mechanics* **13** (1), 8285.
- 1195 KREUZAHLER, S., SCHULZ, D., HOMANN, H., PONTY, Y. & GRAUER, R. 2014 Numerical study
1196 of impeller-driven von kármán flows via a volume penalization method. *New Journal of*
1197 *Physics* **16** (10), 103001.
- 1198 KURIEN, S., L'VOV, V.S, ITAMAR, P. & SREENIVASAN, K.R. 2000 Scaling structure of
1199 the velocity statistics in atmospheric boundary layers. *Physical Review E - Statistical,*
1200 *Nonlinear, and Soft Matter Physics* **61** (1), 407–421.
- 1201 KUZZAY, D., FARANDA, D. & DUBRULLE, B. 2015 Global vs local energy dissipation: The energy
1202 cycle of the turbulent von Kármán flow. *Physics of Fluids* **27** (7), 075105.
- 1203 LAMRIBEN, C., CORTET, P.P. & MOISY, F. 2011 Direct measurements of anisotropic energy
1204 transfers in a rotating turbulence experiment. *Physical Review Letters* **107**, 024503.
- 1205 LAWSON, J.M. 2015 A scanning PIV study of homogeneous turbulence at the dissipation scale.
1206 PhD thesis, University of Cambridge.
- 1207 LAWSON, J.M., BODENSCHATZ, E., KNUTSEN, A.N., DAWSON, J.R & WORTH, N. A. 2019
1208 Direct assessment of kolmogorov's first refined similarity hypothesis. *Physical Review*
1209 *Fluids* **4**.
- 1210 LAWSON, J.M. & DAWSON, J.R. 2014 A scanning PIV method for fine-scale turbulence
1211 measurements. *Experiments in Fluids* **55** (12), 1857.
- 1212 LAWSON, J.M. & DAWSON, J.R. 2015 On velocity gradient dynamics and turbulent structure.
1213 *Journal of Fluid Mechanics* **780**, 60–98.
- 1214 LÓPEZ-CABALLERO, M. & BURGUETE, J. 2013 Inverse cascades sustained by the transfer rate
1215 of angular momentum in a 3d turbulent flow. *Phys. Rev. Lett.* **110**, 124501.
- 1216 LUMLEY, J.L. 1967 Similarity and the turbulent energy spectrum. *The Physics of Fluids* **10** (4),
1217 855–858.
- 1218 MARIÉ, L. & DAVIAUD, F. 2004 Experimental measurement of the scale-by-scale momentum
1219 transport budget in a turbulent shear flow. *Physics of Fluids* **16** (2), 457–461, arXiv:
1220 <https://doi.org/10.1063/1.1637602>.

- 1221 MONCHAUX, R., RAVELET, F., DUBRULLE, B., CHIFFAUDEL, A. & DAVIAUD, F. 2006 Properties
1222 of steady states in turbulent axisymmetric flows. *Physical review letters* **96**, 124502.
- 1223 MONIN, A.S. & YAGLOM, A.M. 1975 *Statistical Fluid Mechanics: Mechanics of Turbulence*.
1224 MIT Press.
- 1225 MORDANT, N., LÉVÊQUE, E. & PINTON, J.F. 2004 Experimental and numerical study of the
1226 lagrangian dynamics of high Reynolds turbulence. *New Journal of Physics* **6**, 116.
- 1227 NI, R. & XIA, K.Q. 2013 Kolmogorov constants for the second-order structure function and
1228 the energy spectrum. *Phys. Rev. E* **87**, 023002.
- 1229 NORE, C., CASTANON, Q.D., CAPPANERA, L. & GUERMOND, J.L. 2018 Numerical simulation
1230 of the von Kármán sodium dynamo experiment. *Journal of Fluid Mechanics* **854**, 164195.
- 1231 NOVARA, MATTEO & SCARANO, FULVIO 2013 A particle-tracking approach for accurate material
1232 derivative measurements with tomographic PIV. *Experiments in Fluids* **54**.
- 1233 OBOUKHOV, A. M. 1962 Some specific features of atmospheric turbulence. *Journal of Fluid*
1234 *Mechanics* **13** (1), 7781.
- 1235 OUELLETTE, N.T., XU, H., M.B. & BODENSCHATZ, E. 2006 An experimental study of turbulent
1236 relative dispersion models. *New Journal of Physics* **8** (6), 109.
- 1237 PAO, Y.H. 1965 Structure of turbulent velocity and scalar fields at large wavenumbers. *Physics*
1238 *of Fluids* **8**.
- 1239 PODVIN, B. & DUBRULLE, B. 2018 Large-scale investigation of a turbulent bifurcation in the
1240 swirling von karman flow. *Fluid Dynamics Research* **50** (6), 065508.
- 1241 POPE, S. B. 2005 *Turbulent flows*. Cambridge: Cambridge Univ. Press.
- 1242 PORTA, A. LA, VOTH, G.A., MOISY, F. & BODENSCHATZ, E. 2000 Using cavitation to measure
1243 statistics of low-pressure events in large-reynolds-number turbulence. *Physics of Fluids*
1244 **12** (6), 1485–1496.
- 1245 PORTELA, F.A., PAPADAKIS, G. & VASSILICOS, J.C. 2017 The turbulence cascade in the near
1246 wake of a square prism. *Journal of Fluid Mechanics* **825**, 315–352.
- 1247 QU, B., BOS, W. & NASO, A. 2017 Direct numerical simulation of axisymmetric turbulence.
1248 *Physical Review Fluids* **2**.
- 1249 RAVELET, FLORENT, MARI, LOUIS, CHIFFAUDEL, ARNAUD & DAVIAUD, F. 2004 Multistability
1250 and memory effect in a highly turbulent flow: Experimental evidence for a global
1251 bifurcation. *Physical review letters* **93**, 164501.
- 1252 RICHARDSON, L. F. 1926 Atmospheric diffusion shown on a distance–neighbour graph. *Royal*
1253 *Society of London Proceedings Series A* **110** (709), 709–737.
- 1254 ROMANO, G.P., ANTONIA, R.A. & ZHOU, T. 1999 Evaluation of LDA temporal and spatial
1255 velocity structure functions in a low reynolds number turbulent channel flow. *Experiments*
1256 *in Fluids* **27** (4), 368–377.
- 1257 SHEN, X. & WARHAFT, Z. 2002 Longitudinal and transverse structure functions in sheared and
1258 unsheared wind-tunnel turbulence. *Physics of Fluids* **14** (1), 370–381.
- 1259 SMITH, L.M. & WALEFFE, F. 1999 Transfer of energy to two–dimensional large scales in forced,
1260 rotating three–dimensional turbulence. *Physics of Fluids* **11** (6), 1608–1622.
- 1261 STEWARTSON, K. 1953 On the flow between two rotating coaxial disks. *Mathematical Proceedings*
1262 *of the Cambridge Philosophical Society* **49** (2), 333–341.
- 1263 THIESSET, F., DANAILA, L., ANTONIA, R.A. & ZHOU, T. 2011 Scale-by-scale energy budgets
1264 which account for the coherent motion. *Journal of Physics: Conference Series* **318** (5),
1265 052040.
- 1266 THORODDSEN, ST 1995 Reevaluation of the experimental support for the kolmogorov refined
1267 similarity hypothesis. *Physics of Fluids* **7** (4), 691–693.
- 1268 VALENTE, P & VASSILICOS, J 2015 The energy cascade in grid-generated non-equilibrium
1269 decaying turbulence. *Physics of Fluids* **27**, 045103.
- 1270 VOTH, G.A, PORTA, A. LA, CRAWFORD, A.M., AELXANDER, J. & BODENSCHATZ, E. 2002
1271 Measurement of particle accelerations in fully developed turbulence. *Journal of Fluid*
1272 *Mechanics* **469**, 121–160.
- 1273 VOTH, G.A., SATYANARAYAN, K. & BODENSCHATZ, E. 1998 Lagrangian acceleration
1274 measurements at large reynolds numbers. *Physics of Fluids* **2268** (10).
- 1275 WANG, C., GAO, Q., WEI, R., LI, T. & WANG, J. 2017 Weighted divergence correction scheme
1276 and its fast implementation. *Experiments in Fluids* **58**, 1–14.

- 1277 WORTH, N. 2010 Tomographic PIV measurement of coherent dissipation scale structures. PhD
1278 thesis, University of Cambridge.
- 1279 WORTH, NA & NICKELS, TB 2011 Time-resolved volumetric measurement of fine-scale coherent
1280 structures in turbulence. *Physical Review E* **84** (2), 025301.
- 1281 YEUNG, PK, DONZIS, DA & SREENIVASAN, KR 2012 Dissipation, enstrophy and pressure
1282 statistics in turbulence simulations at high reynolds numbers. *Journal of Fluid Mechanics*
1283 **700**, 5–15.
- 1284 ZANDBERGEN, P.J. & DIJKSTRA, D. 1987 Von Kármán swirling flows. *Annual Review of Fluid*
1285 *Mechanics* **19** (1), 465–491.